CMS Physics Analysis Summary

Contact: cms-pag-conveners-susy@cern.ch 2021/07/28

Search for higgsinos in channels with two Higgs bosons and missing transverse momentum in proton-proton collisions at $\sqrt{s} = 13\,\text{TeV}$

The CMS Collaboration

Abstract

Results are presented from a search for physics beyond the standard model in proton-proton collisions at $\sqrt{s} = 13\,\text{TeV}$ in final states containing two Higgs bosons, each decaying via the process $\text{H} \to \text{b}\bar{\text{b}}$, and large missing transverse momentum. The search uses a data sample accumulated by the CMS experiment at the CERN LHC corresponding to an integrated luminosity of $137\,\text{fb}^{-1}$. The search is motivated by models of supersymmetry that predict the production of neutralinos, the neutral partners of the electroweak gauge and Higgs bosons. The observed event yields in the signal regions are found to be consistent with the standard model background expectations based on control regions in the data. The results are interpreted using simplified models of supersymmetry. For the electroweak production of nearly degenerate higgsinos, each of whose decay chains yields a neutralino state $\widetilde{\chi}_1^0$ that in turn decays to a massless goldstino and a Higgs boson, $\widetilde{\chi}_1^0$ masses in the range 175 to 1025 GeV are excluded at the 95% confidence level. For the strong production of gluino pairs decaying via a slightly lighter $\widetilde{\chi}_2^0$ to H and a light $\widetilde{\chi}_1^0$, gluino masses below 2330 GeV are excluded.

1 Introduction

The discovery of the Higgs boson H at the LHC [1–4] has provided a new tool for probing physics beyond the standard model (SM). For example, heavy particles that arise in a number of theoretical frameworks could be produced in high energy proton-proton collisions and then decay into Higgs bosons and other particles. A prominent example of such theories is supersymmetry (SUSY) [5–14], which postulates that, for every particle degree of freedom in the SM, there is a corresponding SUSY partner degree of freedom whose spin differs by one-half. Many models based on SUSY can provide solutions to problems and limitations of the SM, both theoretical and empirical.

A major theoretical challenge associated with the SM is the so-called gauge hierarchy problem [15–20], which refers to the instability of the Higgs boson mass against large quantum loop corrections that arise within the SM. In the absence of extreme fine tuning of parameters the Higgs boson mass would be driven up to some high cut-off scale, such as the Planck mass. The degrees of freedom associated with SUSY partners, however, can suppress these quantum corrections, as long as the SUSY particle masses are not too large. Estimates of the maximum degree of SUSY breaking that would still provide a sufficient degree of cancellation of the SM corrections suggest a scale for the lowest mass superpartners roughly on the order of masses kinematically accessible at the LHC [21–23]. A more empirical motivation for SUSY arises from the compelling astrophysical evidence for dark matter. In SUSY models that conserve the R-parity quantum number [11, 24], which is $+1$ for SM particles and -1 for SUSY particles ("sparticles"), the lightest SUSY particle (LSP) would be stable. If the LSP is only weakly interacting, it would provide a potential dark-matter candidate [24].

The minimal supersymmetric extension of the SM (MSSM) includes one additional Higgs doublet of complex scalar fields [12–14]. The superpartners of the SM gauge and higgs bosons are $J = 1/2$ fermions, referred to as gauginos and higgsinos, respectively. The partners of the neutral electroweak gauge and Higgs bosons can in general mix to form a set of electrically neutral mass eigenstates, $\widetilde{\chi}^0_{1\text{-}4}$ (where the particles are ordered in mass, with $\widetilde{\chi}^0_1$ corresponding to the lightest one), referred to as neutralinos, while the charged electroweak gauge and Higgs bosons can mix to form the electrically charged mass eigenstates $\widetilde{\chi}^{\pm}_{1,2}$ [25]. Within these sectors, there are four $J = 1/2$ higgsinos, two charged ($\widetilde{\mathrm{H}}^{\pm}$) and two neutral ($\widetilde{\mathrm{h}}^0$, $\widetilde{\mathrm{H}}^0$). In SUSY models constructed to address the gauge hierarchy problem, the higgsinos are generically among the lightest particles in the spectrum [23].

In SUSY models, a Nambu-Goldstone particle (goldstino, $\widetilde{\mathrm{G}}$) can also appear that is associated with the spontaneous breaking of global supersymmetry and is a fermion. In a broad range of scenarios in which SUSY breaking is mediated at a low scale, such as gauge-mediated symmetry breaking (GMSB) models [26, 27], the goldstino is nearly massless on the scale of the other particles and becomes the LSP.

We describe a search for processes leading to the production of Higgs bosons and LSPs. The LSPs in the models considered here are only weakly interacting and are therefore not detected, leading to an apparent momentum imbalance in the event. The missing momentum transverse to the beam direction, $\vec{p}_{\mathrm{T}}^{\,\mathrm{miss}}$, and its magnitude $p_{\mathrm{T}}^{\mathrm{miss}}$, can be inferred from momentum conservation and are typically large, providing a powerful way to characterize signal events and to suppress SM backgrounds.

The search is designed for sensitivity to several scenarios for the production and decay of SUSY particles. Two scenarios involve the electroweak production of two heavy neutralinos that each decay to a Higgs boson and an LSP. These are a "simplified model" [28–31], TChiHH, in which

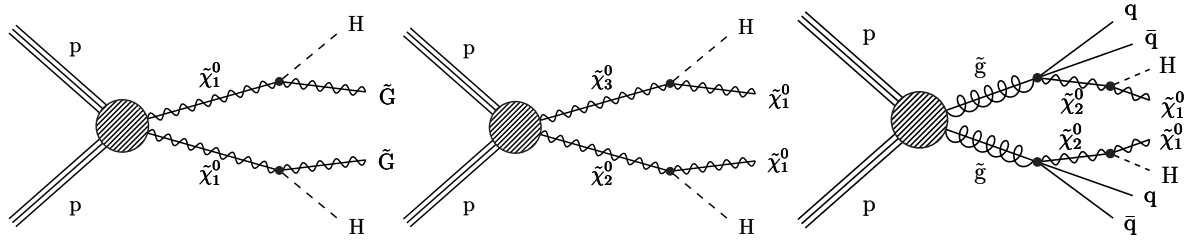

Figure 1: Diagrams for (left) the TChiHH-G signal model, $\widetilde{\chi}_1^0\widetilde{\chi}_1^0 \to \mathrm{HH}\widetilde{\mathrm{G}}\widetilde{\mathrm{G}}$, in which the $\widetilde{\chi}_1^0$ NLSPs are produced indirectly through the cascade decays of several combinations of neutralinos and charginos, as described in the text; (center) TChiHH, in which the electroweak production of two neutralinos leads to two Higgs bosons and two neutralinos ($\widetilde{\chi}_1^0$); (right) T5HH, the strong production of a pair of gluinos, each of which decays via a three-body process to quarks and a neutralino, the neutralino subsequently decaying to a Higgs boson and a $\widetilde{\chi}_1^0$ LSP. In each diagram, the filled circle represents the sum of processes that can lead to the SUSY particles shown.

the LSP is a $\widetilde{\chi}_1^0$, and a more specific GMSB model $\widetilde{\chi}_1^0\widetilde{\chi}_1^0 \to \mathrm{HH}\widetilde{\mathrm{G}}\widetilde{\mathrm{G}}$ [26, 27], in which the LSP is a goldstino; we call the latter TChiHH-G. We also consider the simplified model T5HH, the strong production of a pair of gluinos, each of which decays via a three-body process to quarks and a heavy neutralino, the latter subsequently decaying to a Higgs boson and a $\widetilde{\chi}_1^0$ LSP. Diagrams representing these processes are shown in Fig. 1.

In the TChiHH-G model, Figure 1 (left), the goldstino is the LSP and the $\widetilde{\chi}_1^0$ the next-to-lightest SUSY particle (NLSP) [32]. The NLSPs are produced in the cascade decays of several different combinations of neutralinos and charginos, and the goldstino is taken to be massless. An important scenario arises when the lighter neutralinos $\widetilde{\chi}_{1,2}^0$ and charginos $\widetilde{\chi}_1^\pm$ are dominated by their higgsino content and are thus nearly mass degenerate. In this case, all of their cascade decays can lead to the production of the NLSP and soft particles. Integrating over the contributions from the allowed combinations of produced charginos and neutralinos ($\widetilde{\chi}_1^0\widetilde{\chi}_2^0$, $\widetilde{\chi}_1^0\widetilde{\chi}_1^\pm$, $\widetilde{\chi}_2^0\widetilde{\chi}_1^\pm$, $\widetilde{\chi}_1^\pm\widetilde{\chi}_1^\mp$) leads to an effective rate for $\widetilde{\chi}_1^0\widetilde{\chi}_1^0$ production [33, 34] that is significantly larger than that for any of the individual primary pairs. We assume a branching fraction of 100% for $\widetilde{\chi}_1^0$ to H $\widetilde{\mathrm{G}}$.

Figure 1 (center) corresponds to the more generic model TChiHH, which describes the electroweak production of two higgsinos $\widetilde{\chi}_2^0$ and $\widetilde{\chi}_3^0$. In this model $\widetilde{\chi}_1^0$ is the LSP, assumed to be a bino (the superpartner of the SM boson corresponding to the $U(1)$ weak hypercharge gauge field B), and $\widetilde{\chi}_2^0$ and $\widetilde{\chi}_3^0$, with equal masses, are the NLSPs. Such a mass hierarchy can arise in many scenarios, as discussed in [35, 36]. Unlike in the TChiHH-G scenario described above, we do not assume that the heavier higgsino states always decay to the lightest one, but instead use the higgsino production cross section for only $\widetilde{\chi}_3^0\widetilde{\chi}_2^0$, assuming that we are not sensitive to the other higgsino production combinations ($\widetilde{\chi}_1^\pm\widetilde{\chi}_1^\mp$, $\widetilde{\chi}_1^\pm\widetilde{\chi}_3^0$, and $\widetilde{\chi}_1^\pm\widetilde{\chi}_2^0$). The cross section for $\widetilde{\chi}_3^0\widetilde{\chi}_2^0$ alone is about 17% of that for the sum of all four higgsino cross sections [33, 34].

Because the strong production cross section for gluinos is substantially larger than that of the electroweakinos, many scenarios predict production rates of high-momentum Higgs bosons that are greater in gluino cascade decays than in direct Higgsino production [37, 38]. Figure 1 (right) corresponds to a model (T5HH) in which two gluinos are produced, each of which decays via a three-body process into a quark, an antiquark, and a $\widetilde{\chi}_2^0$. The $\widetilde{\chi}_2^0$ decays into a Higgs boson and a $\widetilde{\chi}_1^0$, which is taken to be the LSP.

2 Analysis strategy

The common signature of the SUSY processes described above is the appearance of two Higgs bosons accompanied by $p_{\mathrm{T}}^{\mathrm{miss}}$. In this search, each Higgs boson is reconstructed in its dominant decay mode, $\mathrm{H} \to \mathrm{b\bar{b}}$, which has a branching fraction of 58% [39]. To provide sensitivity to a wide range of kinematic configurations that arise across the sparticle mass range under study, the analysis uses two approaches to Higgs boson reconstruction. In the resolved phase space region, $\mathrm{H} \to \mathrm{b\bar{b}}$ decays are reconstructed as two separated jets, while in the boosted phase space region, these decays are reconstructed as single jets that have a larger angular spread (wide-cone jets). In both cases, the presence of multiple b-tagged jets is a key part of the signature, and dedicated algorithms are applied to narrow-cone jets (single b tag) and wide-cone jets (double b tag) to enhance the signal purity.

The mass splitting between the higgsino and its sparticle daughter largely determines the momentum of the Higgs boson. This in turn determines whether the resolved or boosted signature will contribute more to the sensitivity. For the resolved signature, the selection limits the overall number of jets present in the event to control the combinatorial background associated with the reconstruction of $\mathrm{H} \to \mathrm{b\bar{b}}$ decays. This selection is designed to target the models with electroweak production, where the jet multiplicity is typically lower than in gluino decays. The boosted selection enhances the sensitivity to models involving electroweak production, particularly for large higgsino masses, and also targets models in which pair-produced gluinos decay via a relatively heavy higgsino.

Events arising from SM processes can sometimes satisfy the $p_{\mathrm{T}}^{\mathrm{miss}}$ requirement of the signal selection, primarily because of neutrinos from W and Z boson decays, and to a lesser extent because of rare extreme mismeasurement of the energies of jets from the copious QCD multijet production (QCD). By imposing a veto on the presence of isolated muons, electrons, or isolated charged tracks, we suppress events with leptonic W boson decays (including those to one-prong hadronically decaying τ leptons), whether the W bosons arise from direct W+jets production or from t quark decays. Backgrounds ("lost lepton") from these events occur when the veto lepton or track is out of acceptance or fails the identification or isolation requirements. Events with decays $\mathrm{Z} \to \nu\bar{\nu}$ also give rise to $p_{\mathrm{T}}^{\mathrm{miss}}$, although Z+jets events containing the required b quark jets are relatively rare.

The search uses an event sample of proton-proton collision data at $\sqrt{s} = 13\,\mathrm{TeV}$, corresponding to an integrated luminosity of $137\,\mathrm{fb}^{-1}$, collected in 2016-18 by the CMS experiment at the CERN LHC. Searches for this and related decay scenarios have been performed by ATLAS [40–57] and CMS [58–83] using 7, 8, and 13 TeV data. The results reported here supersede those of Ref. [65] for the resolved signature and Ref. [71] for the boosted signature, which were based on a subset of the current sample.

3 Detector

A detailed description of the CMS detector, along with a definition of the coordinate system and pertinent kinematic variables, is given in Ref. [84]. Briefly, a cylindrical superconducting solenoid with an inner diameter of 6 m provides a 3.8 T axial magnetic field. Within the cylindrical volume are a silicon pixel and strip tracker, a lead tungstate crystal electromagnetic calorimeter (ECAL), and a brass and scintillator hadron calorimeter (HCAL). The tracking detectors cover the range $|\eta| < 2.5$, where η is the pseudorapidity. The ECAL and HCAL, each composed of a barrel and two endcap sections, cover $|\eta| < 3.0$. Forward calorimeters extend the coverage to $3.0 < |\eta| < 5.2$. Muons are measured within $|\eta| < 2.4$ by gas-ionization

detectors embedded in the steel flux-return yoke outside the solenoid. The detector is nearly hermetic, permitting accurate measurements of $p_{\mathrm{T}}^{\mathrm{miss}}$.

4 Event reconstruction

The reconstruction of physics objects in an event proceeds from the candidate particles identified by the particle-flow (PF) algorithm [85], which uses information from the tracker, calorimeters, and muon systems to identify the candidates as charged or neutral hadrons, photons, electrons, or muons. The transverse momentum of any of these objects is designated p_{T}.

The primary pp interaction vertex is found by taking the reconstructed vertex with the largest value of summed physics-object p_{T}^2. The physics objects for this purpose are the jets (reconstructed using the anti-k_{T} jet finding algorithm [86, 87] with the charged particle tracks assigned to the vertex) and the associated missing transverse momentum (computed as the negative vector sum of the $\vec{p}_{\mathrm{T}}$ values of those jets). Charged particle tracks associated with vertices other than the primary vertex are removed from further consideration. The primary vertex is required to lie within 24 cm of the center of the detector in the direction along the beam axis and within 2 cm in the plane transverse to that axis.

In the event reconstruction, jets are formed from the charged PF candidates associated with the primary vertex, together with the neutral PF candidates, clustered using the anti-k_{T} algorithm [86]. The clustering is performed with distance parameter $R = 0.4$ (AK4 jets) for narrow-cone jets, as implemented in the FASTJET package [87], and with distance parameter $R = 0.8$ (AK8 jets) for wide-cone jets. No removal of overlap jets between the AK4 and AK8 collections is applied, since for the resolved signature the AK8 jets are ignored, while for the boosted signature no restriction on the number of AK4 jets is imposed. Jet quality criteria [88, 89] are imposed to eliminate jets from spurious sources such as electronics noise. The jet energies are corrected for the nonlinear response of the detector [90]. The estimated contribution to the jet p_{T} of neutral PF candidates from extraneous pp interactions (pileup) is removed with a correction based on the area of the jet and the average energy density of the event [91], for AK4 jets, and with the PUPPI technique [92], for AK8 jets. Jets are required to have $|\eta| < 2.4$; AK4 and AK8 jets are required to have $p_{\mathrm{T}} > 30\,\mathrm{GeV}$ and $p_{\mathrm{T}} > 300\,\mathrm{GeV}$, respectively. Finally, AK4 jets that have PF constituents matched to an isolated veto lepton are removed.

The identification of jets originating from b quarks (b jet tagging) is integral to the reconstruction of Higgs bosons in the analysis and is performed separately for AK4 and AK8 jets. For AK4 jets we use a version of the combined secondary vertex algorithm based on deep neural networks (DeepCSV [93]), making use of Loose (L), Medium (M), and Tight (T) working points, as discussed in Section 6. The detection efficiencies for true b quark jets, as well as the mistag rates for up, down, and strange quark and gluon (u d s g) jets, and for charm quark jets, are mildly momentum dependent and are measured in data. The simulation is reweighted to compensate for differences with respect to data based on measurements of the b tagging efficiency and mistag rate for each working point. Typical b jet efficiencies for the three DeepCSV working points are L(85%), M(70%), and T(50%), with corresponding u d s g jet mistag rates of L(10%), M(1%), T (0.1%) and charm jet mistag rates of L(40%), M(12%), and T(2.5%). The numbers of observed b tagged AK4 jets satisfying the L, M, and T requirements in an event are denoted $N_{\mathrm{b,L}}$, $N_{\mathrm{b,M}}$, and $N_{\mathrm{b,T}}$, respectively. The identification of AK8 jets containing two b quarks is performed with a deep-learning-based double-b tagging algorithm (DeepDoubleBvL, mass-decorrelated [94]) at its loose working point. The efficiency for tagging wide-cone jets from $\mathrm{H} \to \mathrm{b\bar{b}}$ is 90%, and for ones containing only u d s g partons is 5%. The number of jets so identified is denoted N_{H}.

The missing transverse momentum, $\vec{p}_{\mathrm{T}}^{\,\mathrm{miss}}$, is given by the negative vector sum of the $\vec{p}_{\mathrm{T}}$ of all PF candidates, adjusted for known detector effects by taking into account the jet energy corrections described in Ref. [95]. Filters are applied to reject events with well defined anomalous sources of $p_{\mathrm{T}}^{\mathrm{miss}}$ arising from calorimeter noise, dead calorimeter cells, beam halo, and other effects.

Because the targeted signature is fully hadronic, contamination from final states involving leptons in the search region is suppressed by vetoing events with reconstructed lepton candidates. Such events often have significant $p_{\mathrm{T}}^{\mathrm{miss}}$ associated with neutrinos, so it is important that such vetos be highly effective. The identification of leptons is also used in the definition of control samples. Electron and muon candidates must satisfy $p_{\mathrm{T}} > 10\,\mathrm{GeV}$ when used to veto events in the search sample, and $p_{\mathrm{T}} > 30\,\mathrm{GeV}$ when used to select events in the single-lepton control samples. For the dilepton control samples, the threshold p_{T} is 30 (20) GeV for the leading (subleading) lepton. Electron and muon candidates must also satisfy $|\eta| < 2.5$ and $|\eta| < 2.4$, respectively.

To improve the quality of the electron reconstruction, additional criteria beyond those of the PF algorithm are imposed on the shower shape in the ECAL and on the ratio of energies associated with the electron candidate in the HCAL and ECAL [96]. For muon candidates [97], more stringent requirements are imposed on the matching between silicon tracker and muon detector track segments.

To preferentially select leptons that originate in the decay of W and Z bosons, suppressing particles misidentified as leptons as well as true leptons produced in decays of hadrons, leptons are required to be isolated from other PF candidates. The isolation criterion is based on the variable I, which is the scalar p_{T} sum of charged hadron, neutral hadron, and photon PF candidates within a cone of radius $\Delta R \equiv \sqrt{(\Delta\phi)^2 + (\Delta\eta)^2}$ around the lepton direction, after pileup subtraction, divided by the lepton p_{T}, where ϕ is the azimuthal angle. The radius of the cone is 0.2 for lepton $p_{\mathrm{T}} < 50\,\mathrm{GeV}$, $10\,\mathrm{GeV}/p_{\mathrm{T}}$ for $50 \leq p_{\mathrm{T}} \leq 200\,\mathrm{GeV}$, and 0.05 for $p_{\mathrm{T}} > 200\,\mathrm{GeV}$. The decrease in cone size with increasing lepton p_{T} accounts for the increased collimation of the decay products from the lepton's parent particle as the Lorentz boost of the parent particle increases [98]. The isolation requirement is $I < 0.1$ (0.2) for electrons (muons).

As discussed in Section 6, a dominant background arises from $\mathrm{t\bar{t}}$ events with a single leptonic decay of a W boson, where the neutrino can produce a significant amount of $p_{\mathrm{T}}^{\mathrm{miss}}$. The lepton can be lost, generating a false all-hadronic signature, either because it is not reconstructed or because it fails the lepton selection requirements (including the p_{T} threshold and isolation requirements), or it can be a tau lepton that decays hadronically. To reduce this background, we veto events with any additional isolated tracks corresponding to leptonic or hadronic PF candidates. To reduce the influence of tracks resulting from pileup, such isolated tracks are considered only if their distance of closest approach along the beam axis to a reconstructed vertex is smaller for the primary vertex than for any other vertex. The tracks are required to satisfy $|\eta| < 2.5$ and $p_{\mathrm{T}} > 10\,\mathrm{GeV}$ ($> 5\,\mathrm{GeV}$ for a PF electron or muon). The isolation requirement is that the scalar p_{T} sum of all other charged particle tracks within a cone of radius 0.3 around the track direction, divided by the track p_{T}, must be less than 0.2 if the track is identified as a PF electron or muon and less than 0.1 otherwise.

Photon candidates, which are used in the selection of a control sample for the study of Z+jets background, are subject to the same calorimeter response criteria as discussed above for electrons. A photon candidate must have no associated response from the pixel tracker. The isolation requirement is based on the individual sums of energy from charged hadrons, neutral hadrons, and electromagnetic particles, excluding the photon candidate itself, within a cone of radius $\Delta R = 0.3$ around the photon candidate's direction, corrected for pileup [96]. Each of the

three individual sums is required to lie below a (different) threshold that depends on whether the photon appears in the barrel or endcap calorimeter.

5 Simulated event samples

While the evaluation of the SM background, described in Section 7, is based primarily on observed event yields in multiple control regions in data, simulated event (MC) samples nevertheless play an important role in the analysis. Such samples are used to optimize the event selection requirements and background prediction methods without biasing the result; to evaluate multiplicative corrections, typically near unity, to the background predictions; and to evaluate the acceptance and efficiency for signal processes.

The SM production of $\mathrm{t\bar{t}}$, W+jets, Z+jets, γ+jets, and QCD events is simulated using the MADGRAPH5_aMC@NLO 2.2.2 (2.4.2) [99, 100] event generator with leading order (LO) precision, for simulation of the data recorded in 2016 (2017–2018). The $\mathrm{t\bar{t}}$ events are generated with up to three additional partons in the matrix element calculations. The W+jets, Z+jets, and γ+jets events are generated with up to four additional partons. Single top quark events produced through the s channel, diboson events such as those originating from WW, ZZ, or ZH production, and rare events such as those from $\mathrm{t\bar{t}W}$, $\mathrm{t\bar{t}Z}$, and WWZ production, are generated, for 2016 (2017–2018), with MADGRAPH5_aMC@NLO 2.2.2 (2.4.2) at next-to-leading order (NLO) [101], except that WW events in which both W bosons decay leptonically are generated using the POWHEG v2.0 [102–106] program at NLO. This same POWHEG generator is used to describe tW production, and t-channel production of single top quark events. The detector response is modeled with GEANT4 [107]. Normalization of the simulated background samples is performed using the most accurate cross section calculations available [99, 105, 106, 108–116], which generally correspond to NLO or next-to-NLO (NNLO) precision.

Samples of simulated signal events are generated at LO using MADGRAPH5_aMC@NLO 2.4.2, with up to two additional partons included in the matrix element calculations. The production cross sections are determined with approximate NNLO plus next-to-next-to-leading logarithmic (NNLL) accuracy [117–128]. For the TChiHH-G model, these samples are generated by performing a scan of $m(\widetilde{\chi}_1^0)$ from threshold to 1500 GeV with $m(\widetilde{\mathrm{G}}) = 1$ GeV. The TChiHH model is represented by a two-dimensional scan of $m(\widetilde{\chi}_1^0)$ from 1 GeV to its kinematic limit, set by $m(\widetilde{\chi}_{2,3}^0)$ which runs from threshold to 1500 GeV. Additional details on the simulation of electroweak production models are given in Ref. [65]. Events with gluino pair production (T5HH) are generated with $m(\widetilde{\mathrm{g}})$ values ranging from 1000–2500 GeV with $m(\widetilde{\chi}_1^0) = 1$ GeV. The mass of the intermediate $\widetilde{\chi}_2^0$ is set 50 GeV below $m(\widetilde{\mathrm{g}})$, ensuring that the daughter Higgs bosons are highly boosted. The gluino decay is simulated with a three-body phase-space model [129].

Because scans over numerous mass points are required for the signal models, the detector response for such events is described using the CMS fast simulation program [129, 130], which yields results that are generally consistent with those from the simulation based on GEANT4. To improve the consistency of the fast simulation description with respect to that based on GEANT4, we apply a correction of 1% to account for differences in the efficiency of the jet quality requirements [88, 89], corrections of 0–12% to account for differences in the modeling of $p_{\mathrm{T}}^{\mathrm{miss}}$, and corrections of up to 1% for differences in the flavor tagging efficiencies.

All simulated samples make use of the PYTHIA 8.205 [131] program to describe parton showering and hadronization. The CUETP8M1 [132] (CP5 [133]) PYTHIA 8.205 tune was used to produce the SM background samples for the analysis of the 2016 (2017 and 2018) data, with signal samples based on the CUETP8M1 tune for 2016 and on the CP2 tune [133] for 2017 and 2018.

Simulated samples generated at LO (NLO) with the CUETP8M1 tune use the NNPDF2.3LO (NNPDF2.3NLO) [134] parton distribution function (PDF), while those using the CP2 or CP5 tune use the NNPDF3.1LO (NNPDF3.1NNLO) [135] PDF. The simulated events are generated with a distribution of pp interactions per bunch crossing that is adjusted to match the corresponding pileup distribution measured in data.

To improve the description of initial-state radiation (ISR), the MADGRAPH5_aMC@NLO prediction is compared with data in a control region enriched in $\mathrm{t\bar{t}}$ events by the requirement of two leptons (ee, $\mu\mu$, or eμ) and two b-tagged jets. The number of all remaining jets in the event is denoted $N_{\mathrm{jet}}^{\mathrm{ISR}}$. A correction factor is applied to simulated $\mathrm{t\bar{t}}$ and strong-production signal events so that the $N_{\mathrm{jet}}^{\mathrm{ISR}}$ distribution agrees with that in data. The correction is found not to be necessary for $\mathrm{t\bar{t}}$ samples that are generated with the CP5 tune, so it is not applied to those samples. The central value of the correction ranges from 0.92 for $N_{\mathrm{jet}}^{\mathrm{ISR}} = 1$ to 0.51 for $N_{\mathrm{jet}}^{\mathrm{ISR}} \geq 6$. The associated systematic uncertainty is taken to be 50% of the correction, accounting for differences between the control samples used to validate the correction and the SM and signal processes to which it is applied. For the electroweak signal samples, we account for the effect of ISR on the p_{T} distribution of the system of SUSY particles, $p_{\mathrm{T}}^{\mathrm{ISR}}$, by reweighting the distribution based on studies of the transverse momentum of Z+jets events [136]. The reweighting factors range between 1.18 at $p_{\mathrm{T}}^{\mathrm{ISR}} \sim 125\,\mathrm{GeV}$ and 0.78 for $p_{\mathrm{T}}^{\mathrm{ISR}} > 600\,\mathrm{GeV}$. We take the deviation from 1.0 as the systematic uncertainty in this reweighting procedure.

Other corrections measured in auxiliary data samples are applied to the simulation to account for differences in factors such as trigger, reconstruction and identification efficiencies, jet energy resolution, and flavor tagging. These are discussed in Sections 4 and 8. The associated systematic uncertainties are applied to the predicted yields specific to the search samples of the analysis.

6 Event selection and reconstruction of Higgs boson candidates

The data sample was obtained using triggers [137, 138] that require $p_{\mathrm{T}}^{\mathrm{miss}}$ to exceed a threshold that varied between 90 and 140 GeV, depending on the LHC instantaneous luminosity. This variable is computed with trigger-level quantities and therefore has somewhat poorer resolution than the corresponding variable used for the offline analysis. The trigger efficiency is measured as a function of the offline $p_{\mathrm{T}}^{\mathrm{miss}}$ and offline H_{T}, the scalar sum of the p_{T} of the accepted AK4 jets, using a sample triggered by a single isolated electron. The efficiency rises with $p_{\mathrm{T}}^{\mathrm{miss}}$ and is over 99% for $p_{\mathrm{T}}^{\mathrm{miss}} > 260\,\mathrm{GeV}$. The resolved signature requires $p_{\mathrm{T}}^{\mathrm{miss}} > 150\,\mathrm{GeV}$ and thus operates partly on the turn-on section of the efficiency curve, while the boosted signature requires $p_{\mathrm{T}}^{\mathrm{miss}} > 300\,\mathrm{GeV}$ and operates on the efficiency plateau. The efficiency turn-on curve is measured separately for each year of data taking.

Several control samples are used to validate the analysis techniques and to estimate systematic uncertainties in the background estimates. Both the resolved and boosted signatures use single-lepton control samples to probe lost-lepton backgrounds. These single-lepton control samples are collected with single-electron, single-muon, and $p_{\mathrm{T}}^{\mathrm{miss}}$ triggers. The resolved signature also uses a dilepton control sample to probe backgrounds arising from $\mathrm{Z} \to \nu\overline{\nu}$ decays. The dilepton control sample is collected with single-electron and single-muon triggers. The boosted signature uses a single-photon control sample to validate $\mathrm{Z} \to \nu\overline{\nu}$ background properties. This sample is obtained using single-photon triggers.

Each signature is analyzed starting with a set of baseline selection requirements. After these selections are applied, further binning in analysis variables is used to increase the sensitivity

to the signal and to provide sidebands for use in background estimation. As noted above, the baseline selection requirements on $p_{\mathrm{T}}^{\mathrm{miss}}$ for the resolved and boosted signatures are $p_{\mathrm{T}}^{\mathrm{miss}} > 150\,\mathrm{GeV}$ and $p_{\mathrm{T}}^{\mathrm{miss}} > 300\,\mathrm{GeV}$, respectively. For both signatures, events are excluded if any veto leptons or isolated charged tracks are present. In the case of isolated charged tracks, we also require the transverse mass m_{T} of the lepton-$\vec{p}_{\mathrm{T}}^{\mathrm{miss}}$ system to satisfy the requirement $m_{\mathrm{T}} < 100\,\mathrm{GeV}$, which serves to limit the veto to likely W boson leptonic decays. To suppress QCD background, events in either signature are rejected if any of the four highest-p_{T} AK4 jets is approximately aligned with the missing momentum vector $\vec{p}_{\mathrm{T}}^{\mathrm{miss}}$. Such alignment is an indication that the observed $\vec{p}_{\mathrm{T}}^{\mathrm{miss}}$ in the event is a consequence of jet mismeasurement and is not genuine. This so-called $\Delta\phi$ requirement can only be imposed in the plane transverse to the beam axis, and the event is vetoed if any of the azimuthal separations is small, specifically, if $\Delta\phi_{\vec{p}_{\mathrm{T}}^{\mathrm{miss}},\mathrm{j}_i} < \{0.5, 0.5, 0.3, 0.3\}$ for the i^{th}-highest p_{T} jet j_i.

For the resolved signature, true signal events have four b jets from the decay of two Higgs bosons, with possible additional jets from initial- or final-state radiation. In addition to the requirements described above, the baseline selection therefore requires that the event contain either 4 or 5 AK4 jets, at least two of which must satisfy tight b-tag requirements. The four jets with the highest b-tag discriminator values are selected and used to form two Higgs boson candidates, each one decaying into two b jets. There are three ways in which these four jets can be assigned to the two Higgs boson candidates. To select one of these three pairs without biasing the mass distributions towards the true Higgs boson mass, we use the pair with the smallest absolute value of the mass difference, Δm_{bb}, between the two candidate masses $m(\mathrm{b}_i\mathrm{b}_j)$ and $m(\mathrm{b}_k\mathrm{b}_l)$, $\Delta m_{\mathrm{bb}} \equiv |m(\mathrm{b}_i\mathrm{b}_j) - m(\mathrm{b}_k\mathrm{b}_l)|$, and require $\Delta m_{\mathrm{bb}} < 40\,\mathrm{GeV}$. This method exploits the fact that signal events contain two particles of identical mass, without using the known value of the Higgs boson mass itself. This method prevents the sculpting of an artificial peak in the background at $m(\mathrm{H})$, which would occur if the value of the Higgs boson mass were used to select the best candidates. The average mass of the two Higgs candidates in the event is required to satisfy $\langle m_{\mathrm{bb}} \rangle < 200\,\mathrm{GeV}$ and is a key analysis variable for the search. Finally, after applying the requirements described above, we consider the angular separation, ΔR, between the b-tagged jets within each Higgs boson candidate. This variable is effective in suppressing the dominant background, which arises from $\mathrm{t\bar{t}}$ production with one hadronic and one leptonic top-quark decay. If the lepton is not detected, with the neutrino supplying the $p_{\mathrm{T}}^{\mathrm{miss}}$, and the two light quarks from a W boson decay are mis-tagged as b jets, then the pairing of the b jet from one t quark with a jet from the other may provide one of the H candidates. However, in such a case ΔR for that candidate will typically be large. This situation is suppressed by requiring $\Delta R_{\mathrm{max}} < 2.2$, where ΔR_{max} is the larger of the ΔR values associated with the two H candidates.

Figure 2 shows the distributions in Δm_{bb}, ΔR_{max}, $\langle m_{\mathrm{bb}} \rangle$, N_{b}, and $p_{\mathrm{T}}^{\mathrm{miss}}$ for both data and simulation, after the baseline selection, together with $N_{\mathrm{b}} \geq 3$, is applied to the resolved-signature analysis variables other than the one shown. Here N_{b} is the number of b-tagged jets, which maps onto non-overlapping $N_{\mathrm{b}} = 2$, 3, and 4 regions, defined as follows: 2b: $N_{\mathrm{b,T}} = 2$, $N_{\mathrm{b,M}} = 2$; 3b: $N_{\mathrm{b,T}} \geq 2$, $N_{\mathrm{b,M}} = 3$, $N_{\mathrm{b,L}} = 3$; 4b: $N_{\mathrm{b,T}} \geq 2$, $N_{\mathrm{b,M}} \geq 3$, $N_{\mathrm{b,L}} \geq 4$.

The boosted signature is designed to select events containing two heavy parent particles, each of which decays into a high-momentum Higgs boson and an undetected particle with large p_{T}. In this kinematic regime, the process $\mathrm{H} \to \mathrm{b\bar{b}}$ leads to a single wide-cone jet that contains the fragmentation and decay products of two b quarks. Thus, the analysis of the boosted signature requires at least two AK8 jets, each with $p_{\mathrm{T}} > 300\,\mathrm{GeV}$ and with a value of the double-b tagging discriminator, D_{bb}, exceeding the loose working point threshold of 0.7. The mass m_{J} attributed to the jet is computed by the "soft drop" algorithm [139, 140], in which soft wide-angle radia-

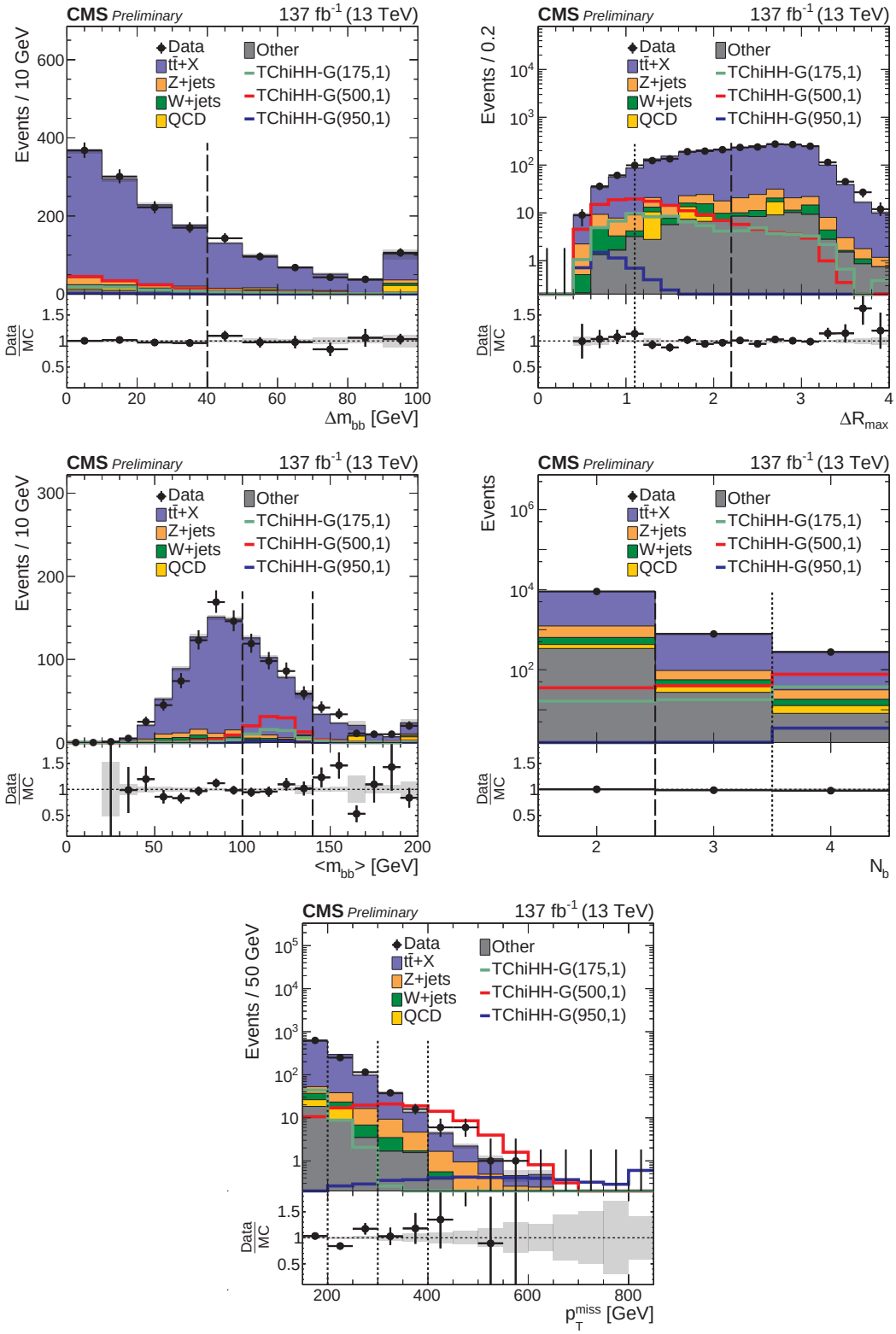

Figure 2: Distributions in the primary variables of the resolved signature for events satisfying the baseline requirements plus $N_{\mathrm{b}} = 3$ or 4, except for those on the variable plotted: (upper left) Δm_{bb}, (upper right) ΔR_{max}, (middle left) $\langle m_{\mathrm{bb}} \rangle$, (middle right) N_{b}, and (lower) $p_{\mathrm{T}}^{\mathrm{miss}}$. The rightmost bin includes overflow entries. The data are shown as black markers with error bars, simulated SM backgrounds by the stacked histograms (scaled by factors of 0.93–0.97 to match the total data yield in each plot), and simulations of TChiHH-G$(m(\widetilde{\chi}_1^0), m(\widetilde{\mathrm{G}}))$ signals by the lines. Gray shading represents the statistical uncertainties of the simulation. Vertical dashed lines indicate the boundaries for SR selection (dashed), or for the SR binning discussed in Section 7 (dotted). The lower panel shows the ratio of data to (scaled) simulation.

tion is recursively removed from a jet. Of these jets, the two with the highest p_{T} are required to have m_{J} in the range $60 < m_{\mathrm{J}} < 260\,\mathrm{GeV}$. The p_{T} threshold applied to the jets results in a high probability that all daughter particles from the Higgs boson decay are contained within the jet cone, and the mass range includes sidebands around the H mass window. The kinematic merging of the Higgs boson decay products in the boosted signature reduces the combinatorial challenge encountered in the resolved signature, and no restriction is needed on the number of AK4 jets. Such jets can arise from initial- or final-state radiation or can be produced in processes involving strongly interacting particles.

Figure 3 shows the distributions for data and simulated event samples with the boosted signature in the event $p_{\mathrm{T}}^{\mathrm{miss}}$, and in p_{T}, m_{J}, and D_{bb} for the two leading AK8 jets. The baseline requirements for the boosted signature are applied, except for those on the variable shown. The simulated event samples show the SM backgrounds, whose distributions are seen to describe the data well. Also shown are examples of SUSY models, which peak around the Higgs boson mass in the m_{J} distributions, and at high values of D_{bb}, for both jets.

In a small region of parameter space a candidate may be selected by both signatures. In this case it is assigned to the resolved signature. Slightly higher expected sensitivity is achieved with this choice than with the alternative.

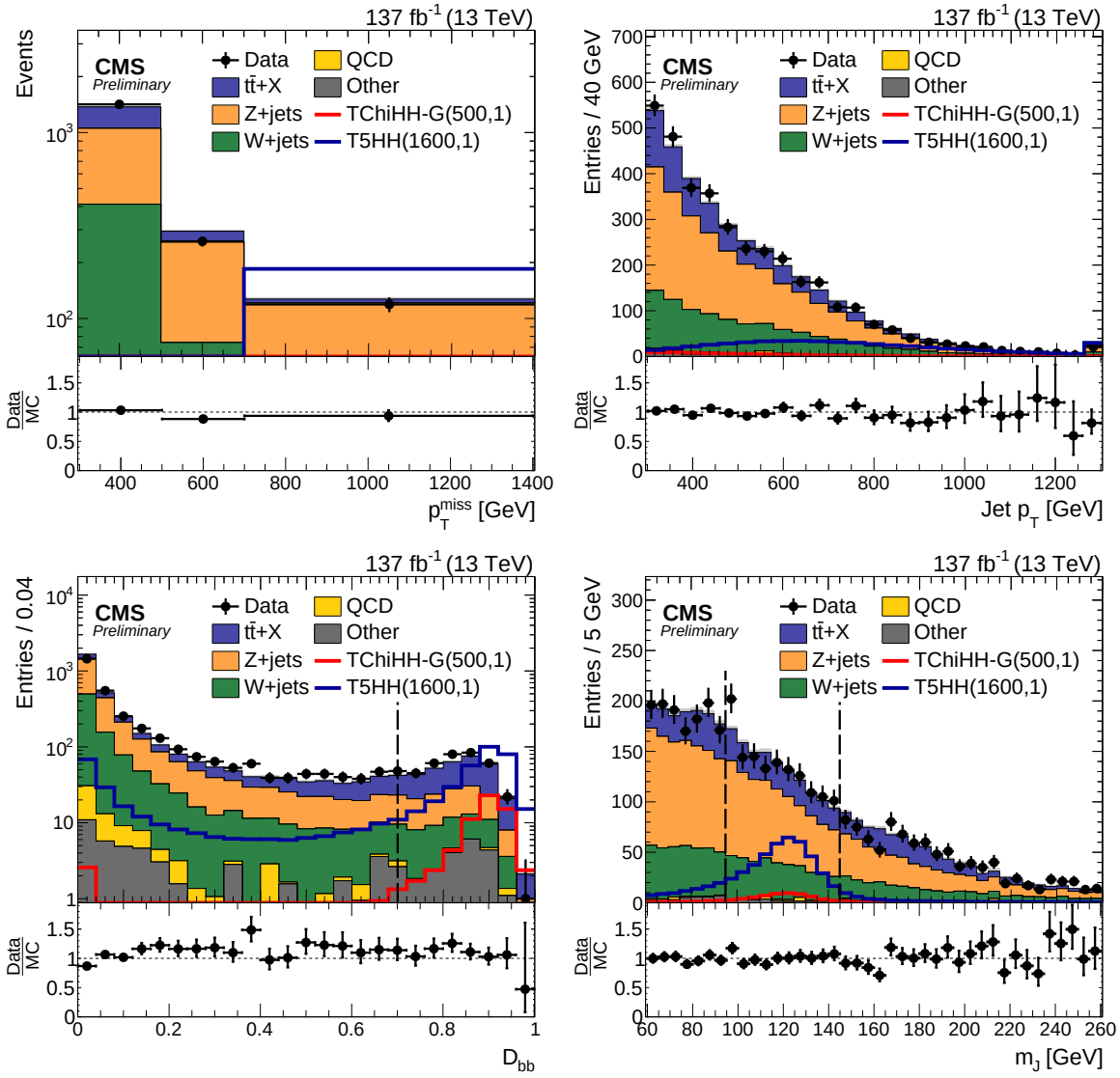

Figure 3: Distributions in the most pertinent variables after the baseline requirements for the boosted signature, except for those on the variable shown: (upper left) $p_{\mathrm{T}}^{\mathrm{miss}}$, (upper right) jet p_{T}, (lower left) D_{bb}, and (lower right) m_{J}. Except for the $p_{\mathrm{T}}^{\mathrm{miss}}$ distribution, each plot contains two entries per event, for each of the two p_{T}-leading wide-cone jets. The data are shown by the black markers with error bars, and SM backgrounds from simulation (scaled by 86% to match the data integral) by the filled histograms. Line histograms show simulations of the signals TChiHH-G$(m(\widetilde{\chi}_1^0), m(\widetilde{\mathrm{G}}))$ or T5HH$(m(\widetilde{\mathrm{g}}), m(\widetilde{\chi}_1^0))$. In the lower-left plot, the vertical dashed line denotes the D_{bb} threshold for classification of the jet as a $\mathrm{H} \to \mathrm{b\bar{b}}$ candidate; in the lower-right plot, the vertical dashed lines denote the boundaries of the H mass window. The lower panel in each plot shows the ratio of observed to (scaled) simulated yields.

7 Event classification and background estimation

After applying the baseline selections for the resolved and boosted signatures, we define the analysis regions shown in Fig. 4 as the basis for an estimate of the SM background yields in the signal regions by the "ABCD method". That is, we use the event yields observed in sideband (SB) and control sideband regions (CSB) to estimate the SM backgrounds in the signal regions (SR). Two types of discriminating variables are used in this procedure: (1) a variable characterizing the H candidate masses ($\langle m_{\mathrm{bb}} \rangle$ for the resolved signature or, for the boosted signature, m_{J_1} and m_{J_2} where by convention J_1 is the p_{T}-leading wide-cone jet), and (2) a variable derived from the jet flavor tagging (N_{b} for the resolved signature or N_{H} for the boosted signature). For the resolved signature, signal events would primarily have four b-tagged jets but can also populate the region with three b-tagged jets, while for the boosted signature, signal events primarily have two identified double-b-tagged jets but can also populate the region with only one. For the resolved signature, signal regions are therefore defined with $N_{\mathrm{b}} = 3$ or 4 and $\langle m_{\mathrm{bb}} \rangle$ in the signal mass window. For the boosted signature, the signal regions are defined with $N_{\mathrm{H}} = 1$ or 2 and with both m_{J_1} and m_{J_2} in the Higgs mass window.

The predicted background yield N_{SR} in a signal region is then estimated from

$$N_{\mathrm{SR}} = \kappa \frac{N_{\mathrm{CSR}}}{N_{\mathrm{CSB}}} N_{\mathrm{SB}}, \tag{1}$$

where N_{SB} is the observed event yield in the H mass sideband for events satisfying the same b tagging criteria as those applied to the signal region, while N_{CSR} and N_{CSB} are, respectively, the event yields in regions corresponding to signal and sideband regions with respect to the Higgs mass variable, but in the background regions with respect to the b tagging criterion. The coefficient κ is a correction factor that takes into account a potential correlation between the two types of discriminating variables. It is taken from simulation but is validated with separate control regions in data, as discussed in Section 8.

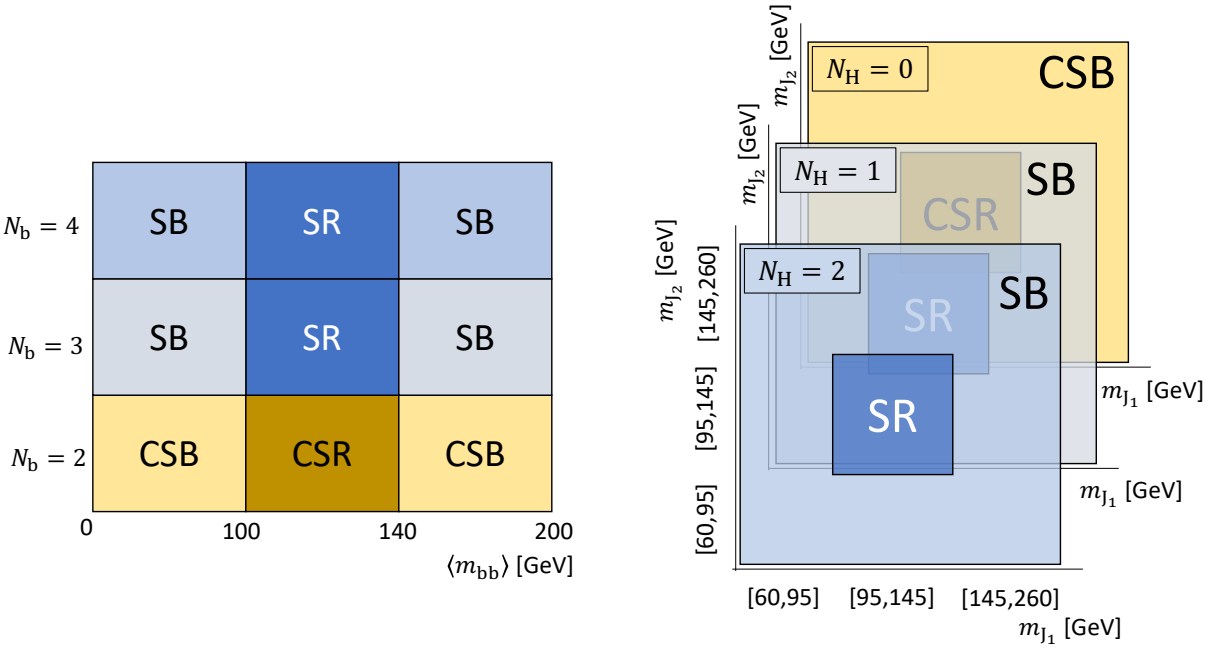

Figure 4: Configuration of the search and control regions for the (left) resolved and (right) boosted signatures. The patterns shown are repeated in each of several bins in kinematic or topological variables for improved sensitivity, as discussed in the text.

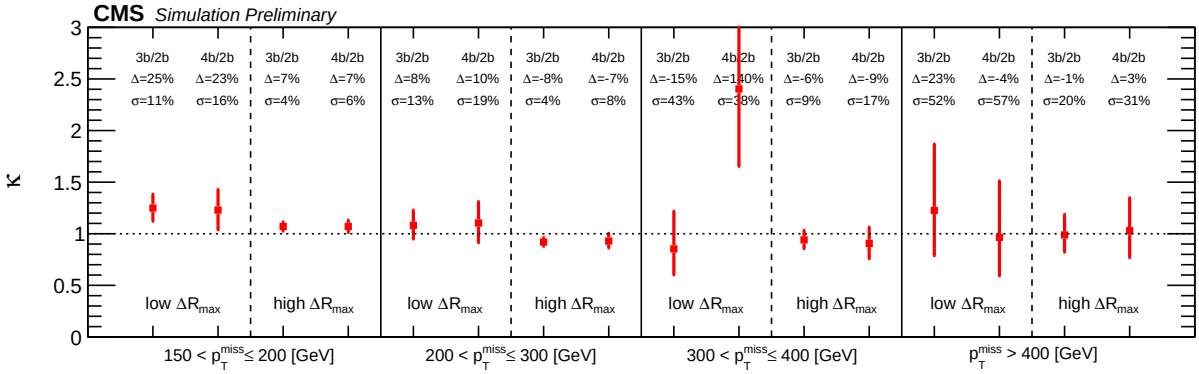

Figure 5: The double ratio $\kappa = (N_{\mathrm{SR}}/N_{\mathrm{SB}})/(N_{\mathrm{CSR}}/N_{\mathrm{CSB}})$ from the SM simulation for the 3b and 4b search samples for each $(p_{\mathrm{T}}^{\mathrm{miss}}, \Delta R_{\mathrm{max}})$ bin of the resolved signature. The value Δ gives the deviation of κ from unity, and σ its relative statistical uncertainty.

For the resolved signature, Fig. 4 (left), the variable N_{b} was defined in Section 6, and the H mass window for the SR or CSR is given by $100 < \langle m_{\mathrm{bb}} \rangle < 140\,\mathrm{GeV}$, with the events both above and below this window constituting the sideband. The SRs and SBs reside in b-tagging regions 3b and 4b, while the 2b region contains the CSR and CSB. To increase the sensitivity to signal, these regions are further sorted into bins in two discriminating variables, ΔR_{max} [0–1.1 and 1.1–2.2] and $p_{\mathrm{T}}^{\mathrm{miss}}$ [150–200, 200–300, 300–400, and $>$400 GeV]. The background determination by the ABCD method is performed separately for each of these eight bins, and for both the 3b and 4b SRs, for a total of 16 bins.

The corresponding ABCD regions for the boosted signature, Fig. 4 (right), are based on N_{H}, with events sorted into regions 0H, 1H, and 2H having $N_{\mathrm{H}} = 0$, 1, and 2 respectively. The SRs and SBs lie within the 1H and 2H regions, and CSR and CSB in 0H. The events in the SR and CSR have $95 < m_{\mathrm{J}} < 145\,\mathrm{GeV}$ for both wide-cone jets, while those in the SB and CSB have at least one of the jets lying outside that mass band, as illustrated in the right-hand plot of Fig. 4. The background yield N_{SR} is determined for each of the 1H and 2H SRs by the ABCD approach. The events in these SRs are further sorted into three $p_{\mathrm{T}}^{\mathrm{miss}}$ bins [300–500, 500–700, and $>$700 GeV], for a total of six bins. The apportionment of the background yield estimate among these $p_{\mathrm{T}}^{\mathrm{miss}}$ bins is discussed below.

The factors κ in Eq. (1) may differ from unity if the H candidate mass variable is correlated with the flavor variable, such that the $N_{\mathrm{SR}}/N_{\mathrm{SB}}$ and $N_{\mathrm{CSR}}/N_{\mathrm{CSB}}$ yield ratios differ. We thus evaluate κ as the double ratio $(N_{\mathrm{SR}}/N_{\mathrm{SB}})/(N_{\mathrm{CSR}}/N_{\mathrm{CSB}})$, taking the yields from simulation. Figure 5 shows the values obtained for κ in each of the 16 analysis bins of the resolved signature. These corrections, with their uncertainties, are applied to the background yield predictions as indicated in Eq. (1). The determination of κ for the boosted signature is illustrated in Fig. 6 (left), which shows the ratio from simulation of the yield in the m_{J} signal band to the yield in the sideband for each of the 0H, 1H, and 2H analysis regions. Dividing this ratio for the 1H (2H) region by the ratio for the 0H region we obtain the corresponding factor, with statistical uncertainties, $\kappa = 1.02 \pm 0.04$ (0.94 ± 0.17). As these are consistent with unity, we set $\kappa = 1$ in the calculation of the central values of the background yields, propagating the uncertainties in κ to these yields. For both signatures systematic contributions to the κ uncertainties are evaluated as discussed in Section 8.

To determine the yield in each $p_{\mathrm{T}}^{\mathrm{miss}}$ bin of the boosted signature, we combine the $p_{\mathrm{T}}^{\mathrm{miss}}$-integrated estimate N_{SR} for the 1H and 2H SRs with the fractional $p_{\mathrm{T}}^{\mathrm{miss}}$ distribution obtained from a sep-

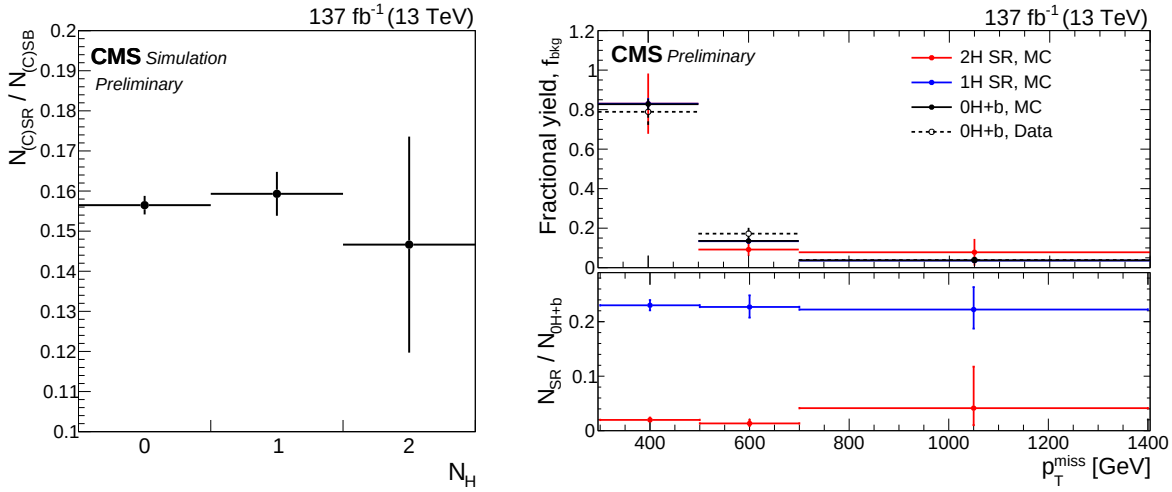

Figure 6: Distributions in (left) the ratio from the SM simulation of the yield in the m_J signal region to the yield in the sideband for each of the 0H, 1H, and 2H analysis regions of the boosted signature, and (right) p_T^{miss} for the 2H and 1H SRs and the 0H+b control region from SM simulation (MC, solid points), and for the control region in data (open black points). In the right-hand plot the upper panel shows the distributions normalized to unit area. The blue points, and in one bin the open point, are hidden under the solid black points. The lower panel shows the (unnormalized) ratios to the 0H+b yields of the SRs 1H (blue) and 2H (red) for the simulation. The error bars show the statistical uncertainties.

arate data control region. This control region is a subsample (0H+b) of 0H events, comprising both the CSR and CSB regions but satisfying the further requirement of one tight b-tagged AK4 jet in addition to the two wide-cone jets. The b-tagging requirement serves to enrich this control sample in $t\bar{t}$ events, so as to approximate the SM content of the 1H and 2H regions. We thus have for the predicted yield, $N_{bkg,i}$, in p_T^{miss} bin i

$$N_{bkg,i} = f_{bkg,i} N_{SR}, \tag{2}$$

where $f_{bkg,i}$ is the fraction of events in the 0H+b sample that fall in p_T^{miss} bin i. We use the SM simulation to test the consistency of the p_T^{miss} distribution in the 0H+b region with those of the 1H and 2H regions. This test is shown in Fig. 6 (right). The ratio distributions in the lower panel are seen to be uniform within the uncertainties of the simulation. This indicates that the 0H+b sample is a valid proxy for the p_T^{miss} shape in the SRs. The figure also shows agreement between the simulation and the fractional distribution f_{bkg} as measured in the data (open points).

8 Background prediction validation and systematic uncertainties

The quantities used for the background estimation that are derived from simulation can be measured in SM-dominated control samples, providing a check on the procedure and estimates of the associated systematic uncertainties. Sections 8.1 and 8.2 describe the evaluation of the background systematic uncertainties for the resolved and boosted signatures, respectively. Section 8.3 describes the systematic uncertainties in the signal model predictions.

8.1 Background systematic uncertainties (resolved signature)

We validate the κ factors described in Sect. 7 and displayed in Fig. 5, and assign systematic uncertainties, by comparing their values obtained in simulation with those from three control samples, each of which is enriched in a specific class of SM background process. The control samples are divided into bins of ΔR_{max} and N_{b}, and for each of these the difference in values of κ between simulation and data is computed. The systematic uncertainty in κ is assigned as the larger between this observed difference and the statistical uncertainty in the value of κ obtained from simulation. The overall uncertainty in κ (in each bin) is based on a weighted sum of the individual values for the three control samples.

The $\mathrm{t\bar{t}}+\mathrm{X}$ systematic uncertainty is measured in a $\mathrm{t\bar{t}}$-dominated single-lepton control sample selected by replacing the lepton and charged track vetoes of the search sample with the requirement of one electron or muon with $p_{\text{T}} > 30\,\text{GeV}$ and no additional muons or electrons. The $\Delta\phi$ requirement is relaxed in the absence of QCD background, to improve the statistical precision, and a requirement $m_{\text{T}} < 100\,\text{GeV}$ is imposed to suppress signal contamination. We find that the data-simulation agreement in κ is consistent across $p_{\text{T}}^{\text{miss}}$ bins, and measure the relative systematic uncertainties in κ for the $\mathrm{t\bar{t}}+\mathrm{X}$ background to be 3% (3b high ΔR_{max}), 10% (4b high ΔR_{max}), 13% (3b low ΔR_{max}) and 18% (4b low ΔR_{max}).

The V+jets systematic uncertainty is measured in a Z+jets dominated dilepton control sample in which we select events with two electrons or muons of opposite sign, at least one of which has $p_{\text{T}} > 30\,\text{GeV}$, dilepton mass between 80 and 100 GeV, and $p_{\text{T}}^{\text{miss}} < 50\,\text{GeV}$. To improve the sample size, we relax the $\Delta\phi$ requirement and extend the range of $p_{\text{T}}(\text{Z})$ (the proxy for $p_{\text{T}}^{\text{miss}}$) down to zero. To reduce $\mathrm{t\bar{t}}$ contamination, we take the CSR and CSB (SR and SB) regions to be defined by the b-jet selection $N_{\text{b,M}} = 0$ (1). We find that the data-simulation agreement in κ is independent of $p_{\text{T}}(\text{Z})$ and measure the relative systematic uncertainties in κ for the V+jets background to be 5% and 16% for the high ΔR_{max} and low ΔR_{max} categories respectively.

The QCD multijet systematic uncertainty is measured in a QCD enriched sample selected by inverting the $\Delta\phi$ requirement of the search sample. As with the dilepton control sample, the CSR and CSB (SR and SB) are defined by the b-jet selection $N_{\text{b,M}} = 0$ (1). We find that data-simulation agreement in κ is independent of $p_{\text{T}}^{\text{miss}}$ and measure the relative systematic uncertainties in κ for the QCD background to be 9% and 7% for the low ΔR_{max} and high ΔR_{max} categories respectively.

The effect of trigger efficiency modeling on κ has been evaluated and found to be negligible ($< 0.1\%$). Table 1 gives a summary of the systematic uncertainties in the backgrounds for the resolved signature. The uncertainties in the separate SM background components are weighted by the relative populations of those components to derive the overall uncertainty from the data-simulation comparisons. The table shows that in most of the SRs the largest contribution to the systematic uncertainty in the background prediction is the statistical uncertainty in the simulation used to determine κ, which ranges from 4 to 57%.

Table 1: Summary of background uncertainties for the resolved signature. The sources are statistical uncertainties in the determination of κ and the uncertainties $\Delta(\text{data, MC})$ derived from the comparison of simulation with data in the single-lepton, dilepton, and low-$\Delta\phi$ control samples. The unit of $p_{\mathrm{T}}^{\mathrm{miss}}$ is GeV, and the last column gives the bin-to-bin correlation ρ.

Source		Uncertainty [%]								ρ
		$150 < p_{\mathrm{T}}^{\mathrm{miss}} \leq 200$		$200 < p_{\mathrm{T}}^{\mathrm{miss}} \leq 300$		$300 < p_{\mathrm{T}}^{\mathrm{miss}} \leq 400$		$p_{\mathrm{T}}^{\mathrm{miss}} > 400$		
		3b	4b	3b	4b	3b	4b	3b	4b	
					Low ΔR_{max}					
κ stat. unc.		11	16	13	19	43	38	52	57	0
	$\mathrm{t\bar{t}}$+X	12	17	10	16	6	12	6	8	1
$\Delta(\text{data, MC})$	V+jets	1	1	4	5	10	6	6	10	1
	QCD	< 1	< 1	< 1	2	< 1	< 1	< 1	< 1	1
					High ΔR_{max}					
κ stat. unc.		4	6	4	8	10	17	20	31	0
	$\mathrm{t\bar{t}}$+X	2	9	2	9	1	8	1	8	1
$\Delta(\text{data, MC})$	V+jets	< 1	< 1	1	< 1	1	1	2	2	1
	QCD	< 1	< 1	< 1	1	< 1	< 1	< 1	1	1

8.2 Background systematic uncertainties (boosted signature)

For the first step of the background evaluation for the boosted signature, extraction of the $p_{\mathrm{T}}^{\mathrm{miss}}$-integrated yields N_{SR} (Eq. 2), the systematic uncertainties are obtained as described above for the resolved signature. A $\mathrm{t\bar{t}}$ and W+jets dominated single-lepton control sample is constructed by modifying the boosted signature search sample selection in the same way as the resolved signature single-lepton control sample. Taking the larger of the data-simulation difference and the statistical uncertainty in that comparison, we find systematic uncertainities of 9% and 13% for the 1H and 2H SRs, respectively. A single-photon sample is used as a cross check on the Z+jets background, but too few events survive the selection, even with enlarged kinematic acceptance, to provide useful measurements of systematic uncertainties. The statistical uncertainty from the calculation of κ in simulation is also assigned as a systematic uncertainty.

The second step is the measurement of the normalized distribution $f_{\mathrm{bkg}}(p_{\mathrm{T}}^{\mathrm{miss}})$ with the 0H+b control region. In simulation we find the ratio between the SR yields and those computed from the sidebands to be independent of $p_{\mathrm{T}}^{\mathrm{miss}}$ within uncertainties. The systematic uncertainty in each $p_{\mathrm{T}}^{\mathrm{miss}}$ bin is taken as the deviation of a linear fit of $f_{\mathrm{bkg}}(p_{\mathrm{T}}^{\mathrm{miss}})$ from the $p_{\mathrm{T}}^{\mathrm{miss}}$-averaged value. The same procedure applied to the single-lepton control sample yields consistent results within large statistical uncertainties. A systematic uncertainty is instead derived from variation of the relative yields of the separate SM contributions in the simulation.

All of these systematic uncertainties in the background yields are summarized in Table 2. The leading contributions are statistical uncertainties in the sideband yields, and those arising from the statistical uncertainties in control sample yields.

Table 2: Summary of systematic uncertainties in the background estimation for the boosted signature alongside the data sideband statistical uncertainties. The values from the ABCD measurement with the p_{T}-integrated sample appear in the rows labeled $p_{\mathrm{T}}^{\mathrm{miss}} > 300\,\mathrm{GeV}$. The row labeled $\Delta(\mathrm{data}, \mathrm{MC})$ gives the contribution derived from the comparison of simulation with data in the one-lepton control sample, and those labeled "MC corrections" refer to the corrections to simulation discussed in Section 5.

Source	$p_{\mathrm{T}}^{\mathrm{miss}}$ (GeV)	Uncertainty (%)	
		1H	2H
Sideband statistics	> 300	10	19
	$[300, 500]$	8	
	$[500, 700]$	18	
	> 700	38	
κ stat. unc.	> 300	4	17
$p_{\mathrm{T}}^{\mathrm{miss}}$ shape closure	$[300, 500]$	2	13
	$[500, 700]$	3	19
	> 700	9	63
$\Delta(\mathrm{data}, \mathrm{MC})$	> 300	9	13
Bkg. composition	$[300, 500]$	3	
	$[500, 700]$	7	
	> 700	32	
MC corrections	> 300	4	6
	$[300, 500]$	1	
	$[500, 700]$	2	
	> 700	5	

8.3 Signal systematic uncertainties

Systematic uncertainties affecting the signal yields from simulation are listed in Table 3. Uncertainties in the modeling of ISR as well as those associated with the usage of the CMS fast simulation program were discussed in Section 5. To evaluate the uncertainty associated with the renormalization (μ_R) and factorization (μ_F) scales, each scale is varied independently by a factor of 2.0 and 0.5 [141–143]. The uncertainty associated with the pileup reweighting is evaluated by varying the value of the total inelastic cross section by 5% [144]. The systematic uncertainty in the determination of the integrated luminosity varies between 1.2 and 2.5% [145–147], depending on the year of data collection. The uncertainties related to the jet energy scale and jet energy resolution are calculated by varying jet properties in bins of p_T and η, according to the uncertainties in the jet energy corrections. The uncertainty on wide-angle jet mass resolution is derived by comparing the mean and width of the W boson peak in the wide-angle jet mass spectrum between data and simulation in a $t\bar{t}$ enriched sample.

The uncertainty in trigger efficiency modeling is derived from the statistical uncertainty in the trigger measurement region, variations in the kinematic selections for the trigger measurement region, and variation in the independent trigger used to measure the efficiency. The resulting systematic uncertainty in the trigger efficiency is 13% or less across all bins; for $p_T^{miss} > 300\,GeV$ the largest uncertainty is 4%.

Systematic uncertainties in the signal predictions and misidentification efficiencies associated with the tagging of b quark jet candidates are evaluated from a sample of data enriched in top quark production. For the study of those associated with the double b tagging of wide-cone jets

Table 3: Sources of systematic uncertainties and their typical impact on the signal yields obtained from simulation. The range is reported as the median 68% among all signal regions for every signal mass point considered. Entries reported as 0 correspond to values smaller than 0.5%.

Source	Relative uncertainty (%)	
	Resolved	Boosted
MC sample statistics	0–18	1–15
ISR modeling	0–2	0–18
Renormalization and factorization scales μ_R and μ_F	0–2	0–7
Pileup corrections	0–2	0–9
Integrated luminosity	1.6	
Jet energy scale	0–7	0–12
Jet energy resolution	0–7	0–7
Trigger efficiency	1-13	0–4
Wide-angle jet mass resolution	—	0–9
b tagging efficiency	2–7	—
b mis-tagging	1–3	—
bb tagging efficiency	—	6–15
Uncertainties attributable to the fast simulation		
Jet quality requirements	1	
p_T^{miss} modeling	0–13	0–12
Wide-angle jet mass resolution	—	2–4
b tagging efficiency	0–1	—
b mis-tagging	0–1	—
bb tagging efficiency	—	< 1

a sample of QCD events enriched in gluons that split into b quark pairs is used. The systematic uncertainties deduced from these studies range from 2 to 7% for jets tagged as b quarks and 6–15% for the double-b tagged jets.

9 Results

The distributions in the appropriate Higgs candidate mass quantity ($\langle m_{\mathrm{bb}} \rangle$ for the resolved signature and m_{J} for the boosted signature) are shown in Figs. 7–9. Figures 7 and 8 show the $\langle m_{\mathrm{bb}} \rangle$ distributiions for the resolved signature in the SR+SB regions of the data, together with the corresponding distributions for the CSR+CSB regions. The latter distributions are corrected with the appropriate values of κ and normalized to the same overall event yield as observed in the SR+SB region. For the boosted signature, Fig. 9 shows the data distributions in m_{J}, and in $(m_{\mathrm{J}_1}, m_{\mathrm{J}_2})$, with simulation overlaid, for the 0H CSR+CSB and the 1H and 2H SR+SB regions, integrated in $p_{\mathrm{T}}^{\mathrm{miss}}$. Systematic uncertainties are not included in these figures, as those uncertainties are computed only for the total yields in the analysis regions. The plots also show representative distributions for potential SUSY signals, with their clear peaks in the H mass band.

To extract the signal yield in each bin, we perform a maximum likelihood fit to the data with a function representing SM yields in each bin plus the yields predicted by a specific model for the signal. The likelihood is a product of Poisson distributions, one for each of the SRs and their corresponding SB, CSR, and CSB regions. Equation (1) is imposed as a constraint on the Poisson means for each of these factors, with the measured value of κ introduced as a Gaussian constraint. Additional Poisson variables represent the three $p_{\mathrm{T}}^{\mathrm{miss}}$ bins of the 0H+b control sample used for the boosted signature. Systematic uncertainties are implemented as additional free parameters with lognormal constraints. Correlations among signal bins are taken into account. The signal yields in the SRs and sidebands are scaled by the strength parameter μ, the ratio of the fitted to theoretical cross section, which allows for signal contamination of the sidebands.

We determine confidence intervals for μ using the test statistic $q_\mu = -2\ln(\mathcal{L}_\mu / \mathcal{L}_{\mathrm{max}})$, where $\mathcal{L}_{\mathrm{max}}$ is the maximum likelihood determined by allowing all parameters including μ to vary, and $\mathcal{L}_\mu$ is the maximum likelihood for a fixed signal strength. Confidence ranges are set under the asymptotic approximation [148], with q_μ approximated with an Asimov data set and used in conjunction with the $\mathrm{CL_s}$ criterion described in Refs. [149, 150].

The observed yields, together with the predicted SM yields, are given in Fig. 10, and in Tables 4 and 5 for the resolved and boosted signatures, respectively. For 15 of the 16 bins of the resolved signature, and the 6 bins of the boosted signature, the distribution of deviations of the observations with respect to SM predictions is consistent with statistical fluctuations. In the single bin corresponding to $\Delta R_{\mathrm{max}} < 1.1$, $N_{\mathrm{b}} = 3$, $300 < p_{\mathrm{T}}^{\mathrm{miss}} < 400\,\mathrm{GeV}$ with the resolved signature, the observed yield is 4 events while the prediction is $0.07^{+0.13}_{-0.05}$ (Table 4). That prediction is based on very small SB and CSR counts (2 events each), leading to highly asymmetric confidence bands. The probability of observing 4 or more events given this background estimate, as measured with a large sample of simulated pseudo-experiments, corresponds to 3.2 standard deviations. The pseudo-experiments were generated with a null model based on the observed sideband yields and associated systematic uncertainties. We have examined the four observed events in detail and find no exceptional features. The models we consider for potential contributions beyond the SM predict that events would be distributed over multiple bins, contrary to the observations here. When we take into account the look-elsewhere effect by considering all 16 bins

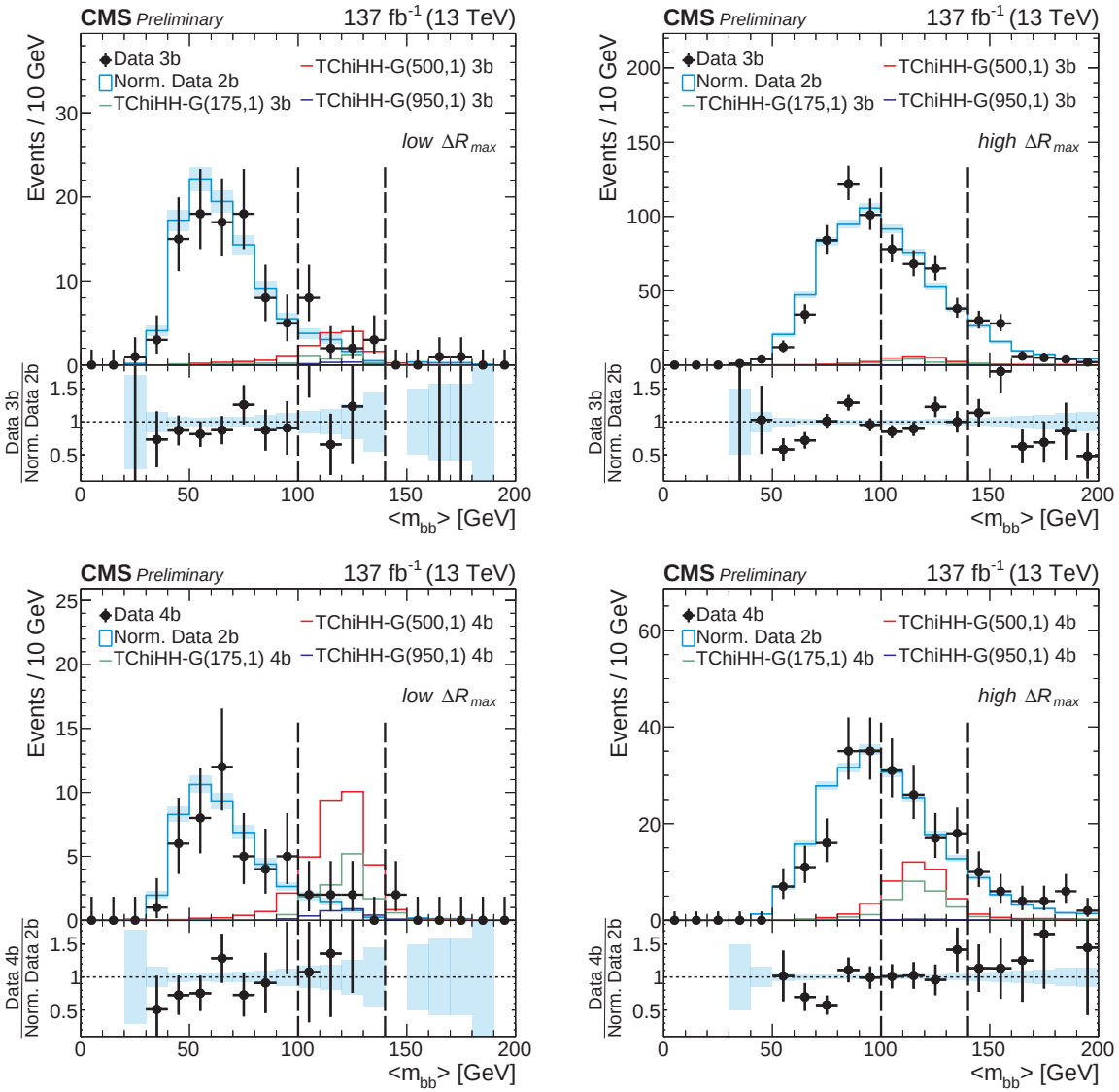

Figure 7: Distributions in $\langle m_{\mathrm{bb}} \rangle$ for (above) 3b and (below) 4b data, denoted by black markers, with error bars indicating the statistical uncertainties. The overlaid cyan histogram shows the corresponding distribution of the 2b data multiplied by κ and scaled in area to the 3b or 4b distribution, with statistical uncertainties indicated by the cyan shading. The ratio of these distributions appears in the lower panel. The red, green, and black histograms show simulations of representative signals, denoted TChiHH-G$(m(\tilde{\chi}_1^0), m(\tilde{\mathrm{G}}))$ in the legends. The left and right plots show the low- and high-ΔR_{max} plane, respectively.

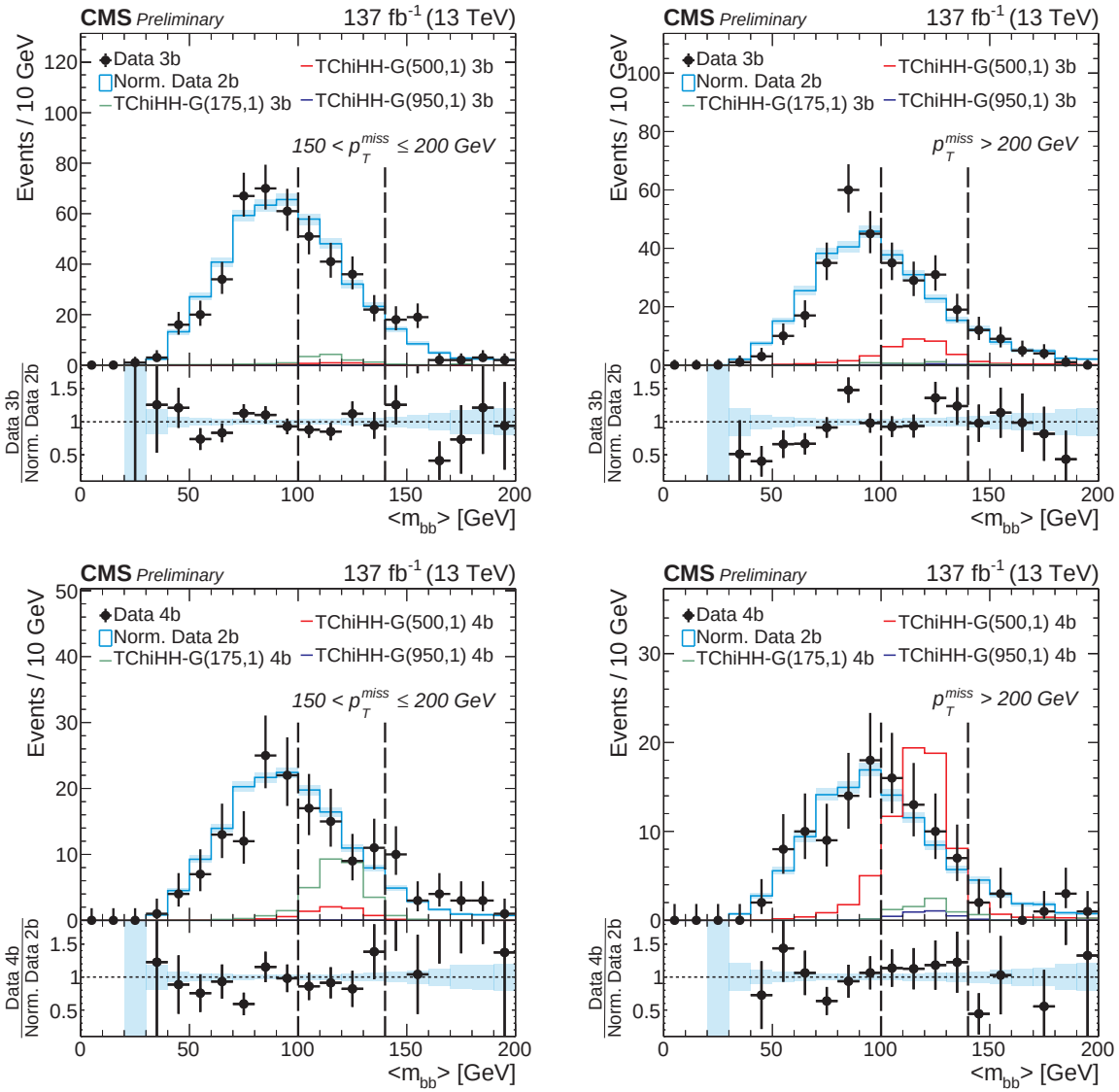

Figure 8: Distributions in $\langle m_{\mathrm{bb}} \rangle$ for (above) 3b and (below) 4b data, denoted by black markers, with error bars indicating the statistical uncertainties. The overlaid cyan histogram shows the corresponding distribution of the 2b data multiplied by κ and scaled in area to the 3b or 4b distribution, with statistical uncertainties indicated by the cyan shading. The ratio of these distributions appears in the lower panel. The red, green, and black histograms show simulations of representative signals, denoted TChiHH-G$(m(\tilde{\chi}_1^0), m(\tilde{\mathrm{G}}))$ in the legends. The left and right plots represent the $p_{\mathrm{T}}^{\mathrm{miss}} < 200\,\mathrm{GeV}$ and $p_{\mathrm{T}}^{\mathrm{miss}} \geq 300\,\mathrm{GeV}$ plane, respectively.

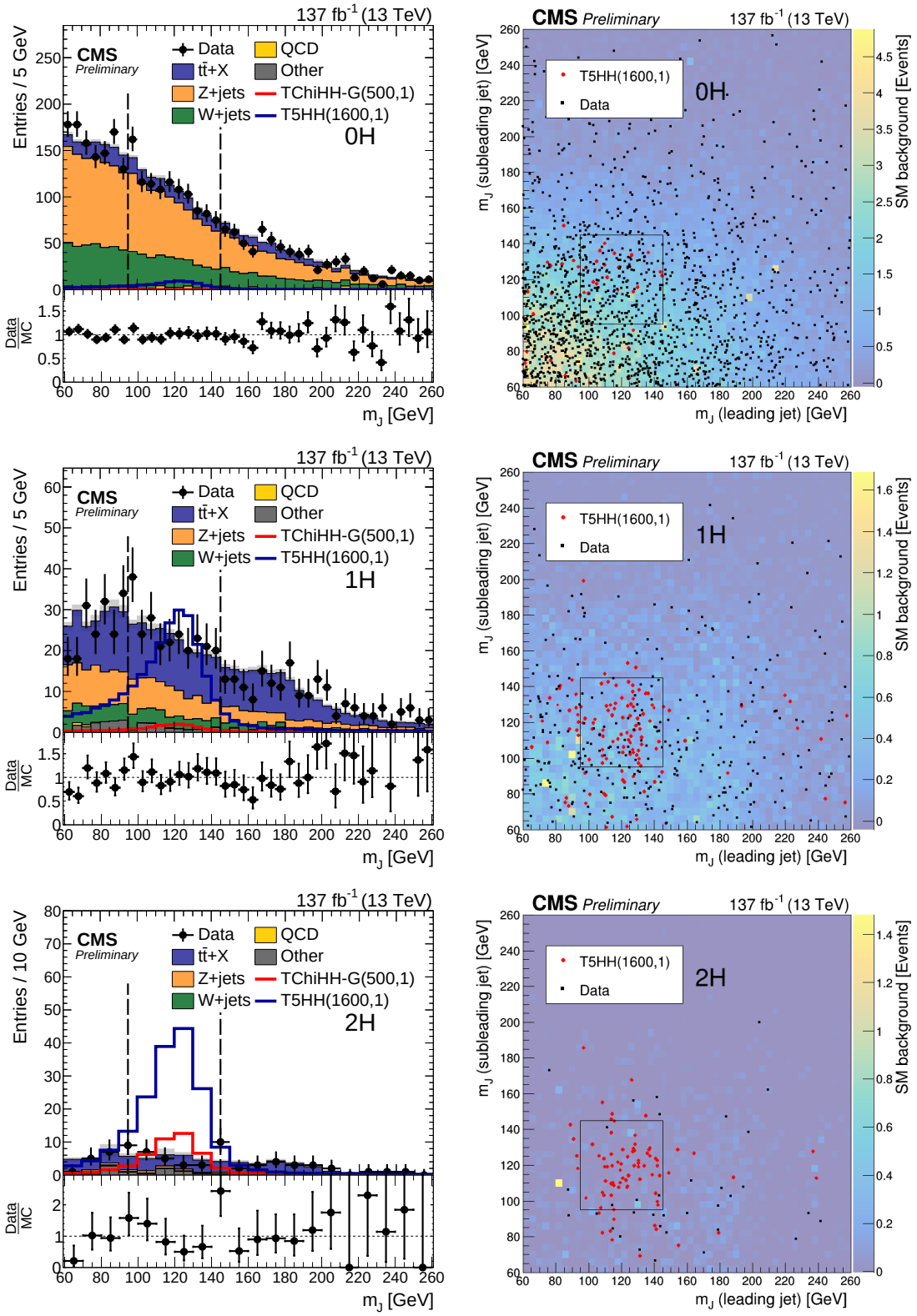

Figure 9: Distributions in m_J for the boosted signature, integrated in p_T^{miss}. The projections (left) contain two entries per event, with statistical uncertainties in the data and simulation given by the vertical bars and gray shading, respectively. The SM components are scaled to the data integral, by factors of 0.84, 0.92, and 1.13 in the 0H (upper), 1H (middle), and 2H (lower) plot, respectively. The data to simulation ratio appears in each lower panel. Simulated signals TChiHH-G$(m(\tilde{\chi}_1^0), m(\tilde{G}))$ and T5HH$(m(\tilde{g}), m(\tilde{\chi}_1^0))$ are also shown. In the correlation plots (right) the continuous color scale represents the SM background, black dots the data, and red dots the expected signal. The dashed lines and box denote the boundaries of the SR.

Table 4: For each SR of the resolved signature, the MC closure factor κ, predicted background yield N_{bkg} (pre-fit), background yield from the background-only fit N_{bkg} (post-fit), and observed yield N_{obs}. The first and second uncertainties in the κ factors are statistical and systematic, respectively. The uncertainties in the predictions, extracted from the maximum-likelihood fit described in the text, include both statistical and systematic contributions. The interpretation of results in the bin corresponding to $\Delta R_{\text{max}} < 1.1$, $N_{\text{b}} = 3$, $300 < p_{\text{T}}^{\text{miss}} < 400\,\text{GeV}$ is discussed in the text.

ΔR_{max}	N_{b}	$p_{\text{T}}^{\text{miss}}$ [GeV]	κ	N_{bkg}		N_{obs}
				Pre-fit	Post-fit	
1.1–2.2	3	150–200	$1.07 \pm 0.04 \pm 0.02$	159 ± 13	$150.5^{+8.8}_{-8.5}$	141
		200–300	$0.92 \pm 0.04 \pm 0.02$	$91.3^{+9.8}_{-9.0}$	$92.1^{+6.9}_{-6.5}$	91
		300–400	$0.94^{+0.09}_{-0.08} \pm 0.01$	$11.1^{+3.3}_{-2.7}$	$12.5^{+2.6}_{-2.2}$	14
		> 400	$0.99^{+0.20}_{-0.17} \pm 0.02$	$2.8^{+2.4}_{-1.4}$	$2.8^{+1.4}_{-1.0}$	3
	4	150–200	$1.07 \pm 0.06 \pm 0.10$	$50.7^{+8.2}_{-7.2}$	$51.7^{+5.4}_{-5.0}$	51
		200–300	$0.93 \pm 0.07 \pm 0.08$	$27.7^{+5.7}_{-4.9}$	$32.6^{+4.3}_{-3.9}$	37
		300–400	$0.91^{+0.16}_{-0.15} \pm 0.07$	$2.7^{+1.6}_{-1.1}$	$3.3^{+1.3}_{-1.0}$	4
		> 400	$1.03^{+0.32}_{-0.26} \pm 0.09$	$2.9^{+2.7}_{-1.5}$	$1.34^{+1.03}_{-0.66}$	0
< 1.1	3	150–200	$1.25 \pm 0.13 \pm 0.15$	$6.0^{+1.7}_{-1.3}$	$6.9^{+1.5}_{-1.3}$	9
		200–300	$1.08^{+0.14}_{-0.13} \pm 0.12$	$1.97^{+0.74}_{-0.56}$	$2.18^{+0.70}_{-0.55}$	2
		300–400	$0.85^{+0.36}_{-0.25} \pm 0.10$	$0.07^{+0.13}_{-0.05}$	$0.78^{+0.58}_{-0.36}$	4
		> 400	$1.23^{+0.64}_{-0.44} \pm 0.10$	$0.87^{+1.30}_{-0.58}$	$0.50^{+0.62}_{-0.33}$	0
	4	150–200	$1.23^{+0.20}_{-0.19} \pm 0.21$	$2.55^{+0.98}_{-0.74}$	$2.52^{+0.81}_{-0.64}$	1
		200–300	$1.10^{+0.21}_{-0.19} \pm 0.19$	$0.96^{+0.49}_{-0.34}$	$1.33^{+0.55}_{-0.41}$	3
		300–400	$2.40^{+0.91}_{-0.75} \pm 0.32$	$0.42^{+0.61}_{-0.27}$	$1.15^{+0.86}_{-0.54}$	1
		> 400	$0.96^{+0.55}_{-0.37} \pm 0.12$	$0.65^{+2.29}_{-0.44}$	$0.65^{+1.18}_{-0.31}$	1

Table 5: For each N_{H} SR of the boosted signature, the total predicted background yield N_{SR}, and for each $p_{\text{T}}^{\text{miss}}$ bin the fraction f_{bkg}, both with their statistical uncertainties, the predicted background yield N_{bkg}–pre-fit, the yield from the background-only fit N_{bkg}–post-fit, and the observed yield N_{obs}. Both N_{SR} and f_{bkg} are determined from data control samples. The N_{bkg} values are extracted from the maximum-likelihood fit described in the text, with uncertainties that include both statistical and systematic contributions.

N_{H}	$p_{\text{T}}^{\text{miss}}$ [GeV]	N_{SR}	f_{bkg}	N_{bkg}		N_{obs}
				Pre-fit	Post-fit	
1	300–500	42.9 ± 4.2	0.789 ± 0.030	$33.6^{+6.1}_{-5.2}$	$37.0^{+4.2}_{-4.0}$	42
	500–700		0.172 ± 0.028	$7.3^{+2.0}_{-1.6}$	$7.2^{+1.5}_{-1.3}$	6
	> 700		0.039 ± 0.014	$1.65^{+1.04}_{-0.66}$	$1.50^{+0.75}_{-0.53}$	1
2	300–500	5.1 ± 1.0	0.789 ± 0.030	$4.0^{+1.5}_{-1.1}$	$4.0^{+1.2}_{-1.0}$	4
	500–700		0.172 ± 0.028	$0.88^{+0.40}_{-0.28}$	$0.74^{+0.29}_{-0.21}$	0
	> 700		0.039 ± 0.014	$0.20^{+0.21}_{-0.10}$	$0.14^{+0.13}_{-0.07}$	0

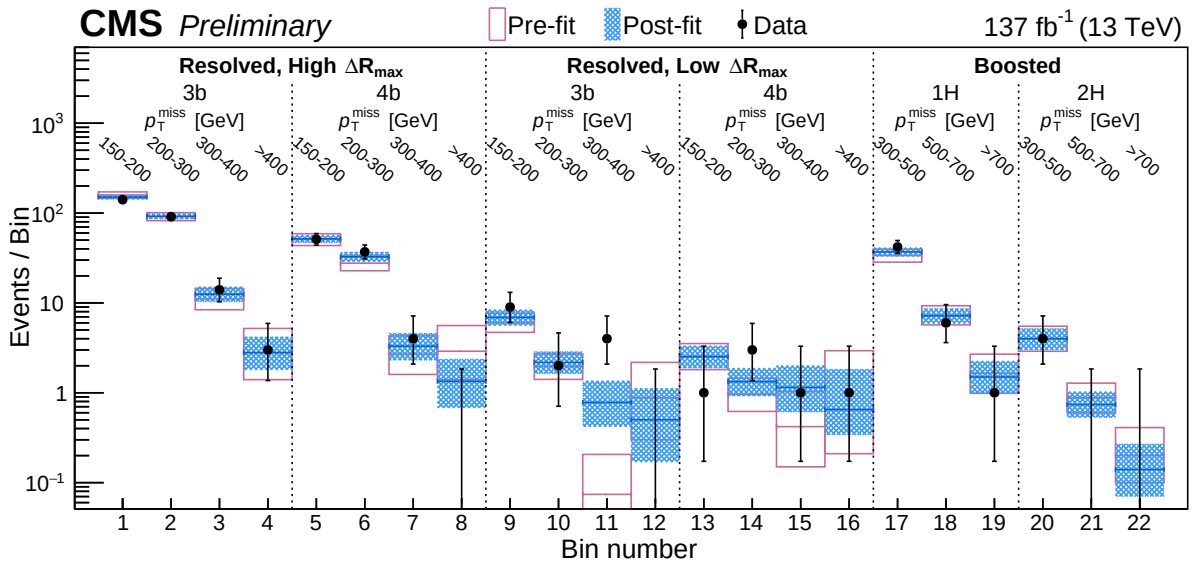

Figure 10: Observed and predicted yields in the search regions identified by the legend text. The points with error bars represent the observed yields, the magenta outline bands the background yields derived from the data sidebands with their total uncertainty, and blue shaded bands the values determined by the background-only fit.

of the resolved signature, the resulting global p-value corresponds to 1.9 standard deviations.

We interpret the data in terms of the three models discussed in Section 1. In each case the data from both resolved and boosted signatures are included in the fit. Fig. 11 shows the limit on the cross section at 95% CL for the TChiHH-G model of Fig. 1 (left). For the case of degenerate intermediate higgsinos the data exclude masses of the $\widetilde{\chi}_1^0$ in the range 175 to 1025 GeV. If instead only the $\widetilde{\chi}_2^0$ intermediate state is kinematically accessible, the data do not exclude the model. The highest sensitivity is attained around $250 < m(\widetilde{\chi}_1^0) < 500$ GeV, where the single-bin excess noted above leads to a limit less restrictive than the expected one.

For the TChiHH model (Fig. 1, center) the cross section limit is presented in Fig. 12 as a function of independent masses $m(\widetilde{\chi}_2^0)$ and $m(\widetilde{\chi}_1^0)$. While the expected limit would exclude a substantial region of this plane, there is no observed exclusion, again because of the single-bin excess.

For the T5HH model (Fig. 1, right) of gluino pair production with a $\widetilde{\chi}_2^0$ NLSP slightly less massive than the gluino and a light LSP, masses $m(\widetilde{\mathrm{g}}) < 2330$ GeV are excluded.

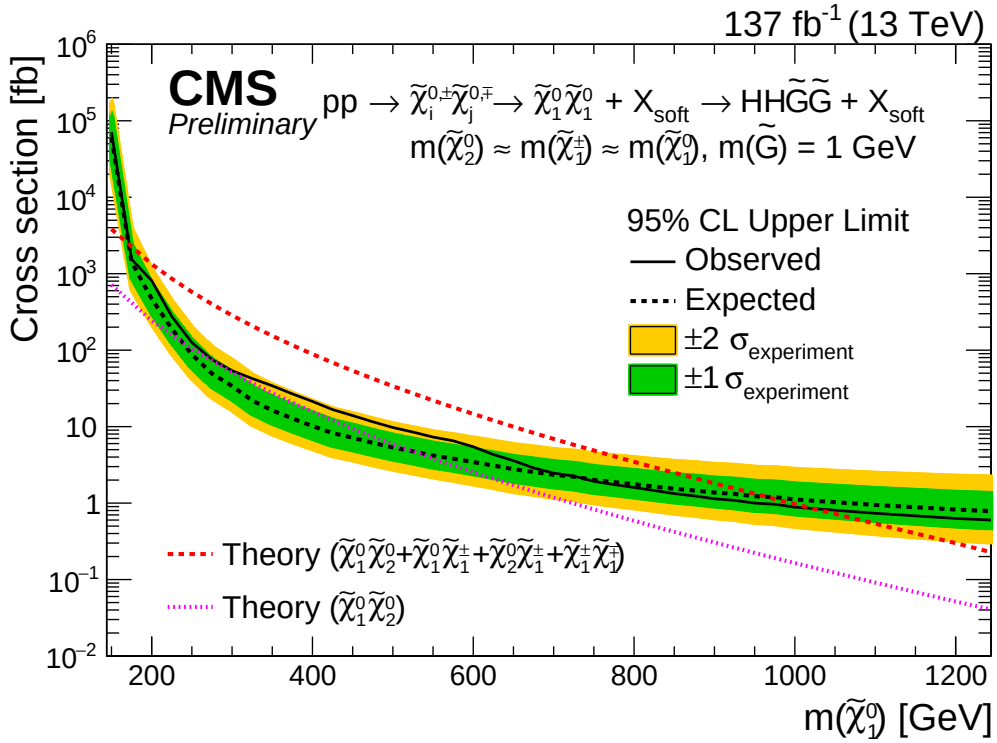

Figure 11: Observed and expected upper limits at 95% CL on the cross section for the gauge-mediated symmetry breaking signal model $\tilde{\chi}_1^0\tilde{\chi}_1^0 \to \mathrm{HH}\tilde{\mathrm{G}}\tilde{\mathrm{G}}$. The thin dashed black line with green and yellow bands shows the expected limit with its 1- and 2-standard deviation uncertainties, while the solid black line shows the observed limit. The theoretical cross section is indicated by the dashed red line under the assumption that the decay chains leading to the $\tilde{\chi}_1^0\tilde{\chi}_1^0$ intermediate state include a degenerate set of all charginos and neutralinos, and by the dotted magenta lines under the assumption that only the combination $\tilde{\chi}_1^0\,\tilde{\chi}_2^0$ is accessible.

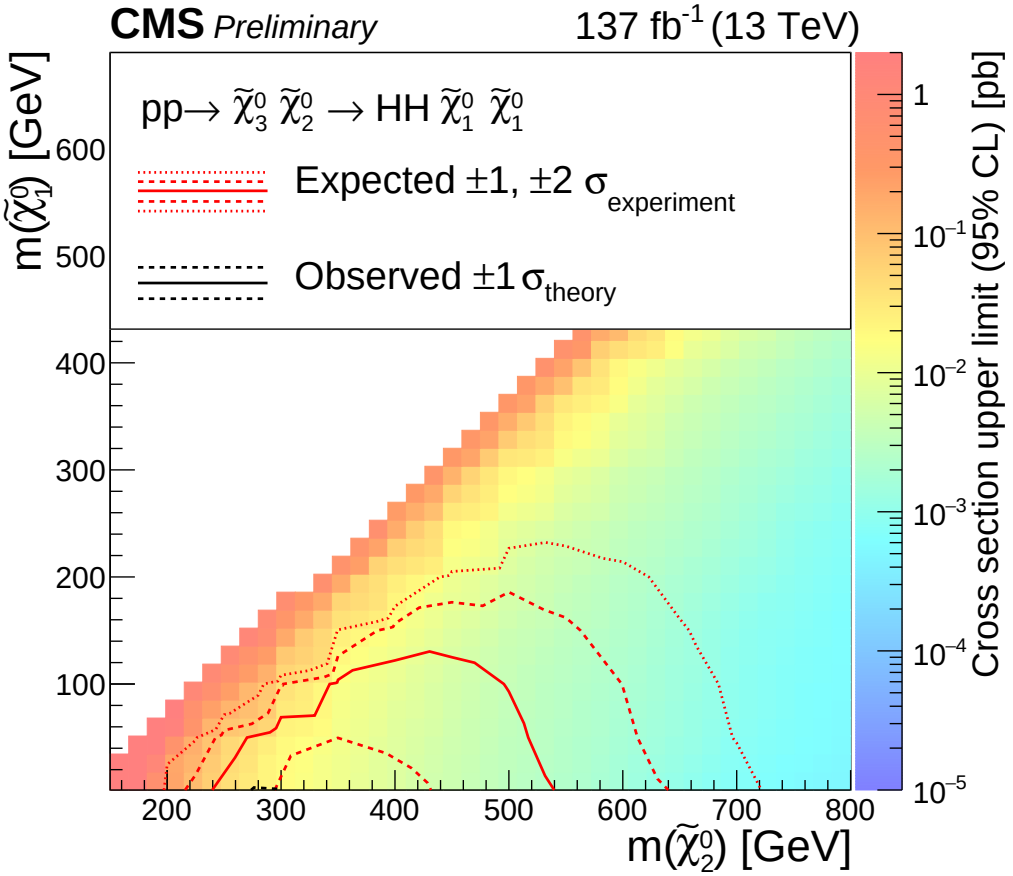

Figure 12: Limits at 95% CL on the cross section for the TChiHH signal model in which production of the intermediate state $\tilde{\chi}_2^0\,\tilde{\chi}_3^0$ (assumed mass degenerate) is followed by the decay of each to $\tilde{\chi}_1^0$ H. The color scale gives the cross section limit as a function of $(m(\tilde{\chi}_2^0), m(\tilde{\chi}_1^0))$. The red solid and dashed contours show the expected limit with its 1-standard deviation uncertainty. At its central value the observed cross section surface does not exclude any part of the plane for this model; only the +1-standard deviation (dashed black) surface intersects the theoretical cross section, near $m(\tilde{\chi}_2^0) = 300\,\text{GeV}$ for the smallest values of $m(\tilde{\chi}_1^0)$.

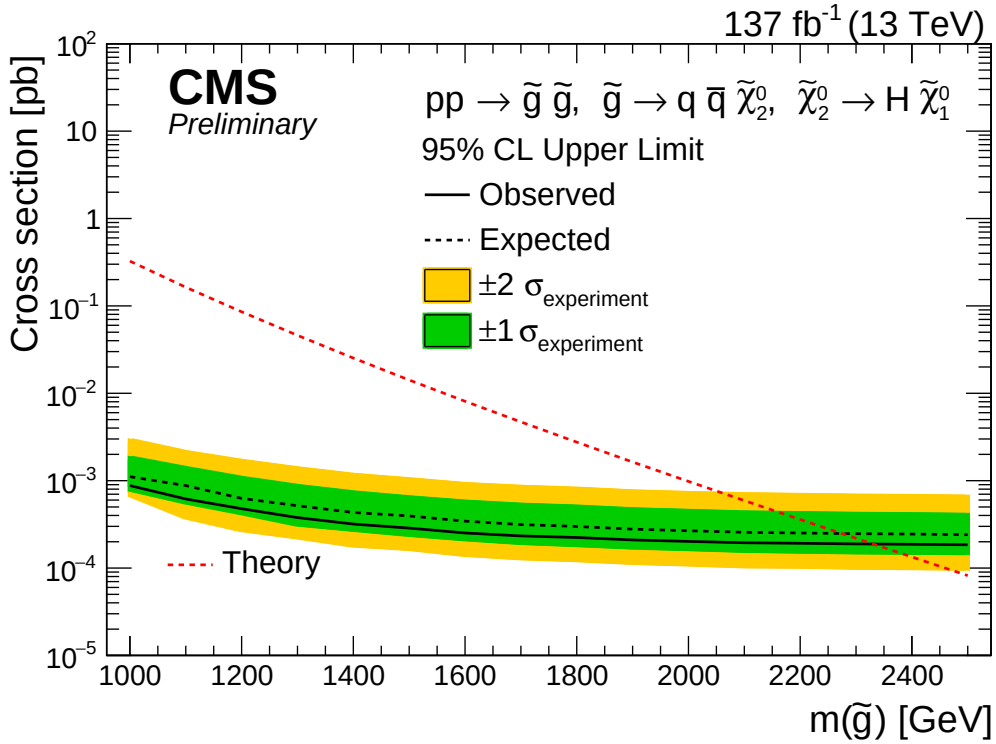

Figure 13: Observed and expected upper limits at 95% CL on the cross section for the simplified model T5HH, the strong production of a pair of gluinos each of which decays via a three-body process to quarks and a neutralino, the neutralino subsequently decaying to a Higgs boson and a $\widetilde{\chi}_1^0$ LSP. The thin dashed black line with green and yellow bands shows the expected limit with its 1- and 2-standard deviation uncertainties; the solid black line shows the observed limit, and the dashed red line the theoretical cross section.

10 Summary

A search is presented for physics beyond the standard model in final states with pairs of Higgs bosons and an imbalance of transverse momentum, produced in proton-proton collisions at $\sqrt{s} = 13\,\text{TeV}$. The data, collected by the CMS experiment at the LHC, correspond to an integrated luminosity of $137\,\text{fb}^{-1}$. The Higgs bosons are reconstructed via their decay to a pair of b quarks, observed either as distinct b quark jets or as wide-cone jets each containing the pair of b quarks. No significant excess of events beyond those predicted by standard model processes is observed. This finding is used to set limits on the cross sections for the production of SUSY particles, considering both the direct production of neutralinos and their production through intermediate states with gluinos.

For the electroweak production of nearly-degenerate higgsinos each of whose decay cascades yield a $\widetilde{\chi}_1^0$ that in turn decays through a Higgs boson to the lightest SUSY particle (LSP), a massless goldstino, $\widetilde{\chi}_1^0$ masses in the range 175 to 1025 GeV are excluded at the 95% confidence level. For a model with a mass splitting between the directly produced higgsinos and a bino LSP, the cross section upper limit lies slightly above the model cross section over the entire mass-parameter region where the experiment has expected sensitivity. For the strong production of gluino pairs decaying via a slightly lighter $\widetilde{\chi}_2^0$ to a Higgs boson and a light $\widetilde{\chi}_1^0$ LSP, gluino masses below 2330 GeV are excluded.

References

[1] ATLAS Collaboration, "Observation of a new particle in the search for the standard model Higgs boson with the ATLAS detector at the LHC", *Phys. Lett. B* **716** (2012) 1, doi:10.1016/j.physletb.2012.08.020, arXiv:1207.7214.

[2] CMS Collaboration, "Observation of a new boson at a mass of 125 GeV with the CMS experiment at the LHC", *Phys. Lett. B* **716** (2012) 30, doi:10.1016/j.physletb.2012.08.021, arXiv:1207.7235.

[3] CMS Collaboration, "Observation of a new boson with mass near 125 GeV in pp collisions at $\sqrt{s}$ = 7 and 8 TeV", *JHEP* **06** (2013) 081, doi:10.1007/JHEP06(2013)081, arXiv:1303.4571.

[4] ATLAS and CMS Collaborations, "Combined measurement of the Higgs boson mass in pp collisions at $\sqrt{s} = 7$ and 8 TeV with the ATLAS and CMS experiments", *Phys. Rev. Lett.* **114** (2015) 191803, doi:10.1103/PhysRevLett.114.191803, arXiv:1503.07589.

[5] P. Ramond, "Dual theory for free fermions", *Phys. Rev. D* **3** (1971) 2415, doi:10.1103/PhysRevD.3.2415.

[6] Y. A. Golfand and E. P. Likhtman, "Extension of the algebra of Poincaré group generators and violation of P invariance", *JETP Lett.* **13** (1971) 323.

[7] A. Neveu and J. H. Schwarz, "Factorizable dual model of pions", *Nucl. Phys. B* **31** (1971) 86, doi:10.1016/0550-3213(71)90448-2.

[8] D. V. Volkov and V. P. Akulov, "Possible universal neutrino interaction", *JETP Lett.* **16** (1972) 438.

[9] J. Wess and B. Zumino, "A Lagrangian model invariant under supergauge transformations", *Phys. Lett. B* **49** (1974) 52, doi:10.1016/0370-2693(74)90578-4.

[10] J. Wess and B. Zumino, "Supergauge transformations in four dimensions", *Nucl. Phys. B* **70** (1974) 39, doi:10.1016/0550-3213(74)90355-1.

[11] P. Fayet, "Supergauge invariant extension of the Higgs mechanism and a model for the electron and its neutrino", *Nucl. Phys. B* **90** (1975) 104, doi:10.1016/0550-3213(75)90636-7.

[12] P. Fayet and S. Ferrara, "Supersymmetry", *Phys. Rept.* **32** (1977) 249, doi:10.1016/0370-1573(77)90066-7.

[13] H. P. Nilles, "Supersymmetry, supergravity and particle physics", *Phys. Rep.* **110** (1984) 1, doi:10.1016/0370-1573(84)90008-5.

[14] S. P. Martin, "A supersymmetry primer", *Adv. Ser. Direct. High Energy Phys.* **21** (2010) 1, doi:10.1142/9789814307505_0001, arXiv:hep-ph/9709356.

[15] G. 't Hooft, "Naturalness, chiral symmetry, and spontaneous chiral symmetry breaking", *NATO Sci. Ser. B* **59** (1980) 135, doi:10.1007/978-1-4684-7571-5_9.

[16] E. Witten, "Dynamical breaking of supersymmetry", *Nucl. Phys. B* **188** (1981) 513, doi:10.1016/0550-3213(81)90006-7.

[17] M. Dine, W. Fischler, and M. Srednicki, "Supersymmetric technicolor", *Nucl. Phys. B* **189** (1981) 575, doi:10.1016/0550-3213(81)90582-4.

[18] S. Dimopoulos and S. Raby, "Supercolor", *Nucl. Phys. B* **192** (1981) 353, doi:10.1016/0550-3213(81)90430-2.

[19] S. Dimopoulos and H. Georgi, "Softly broken supersymmetry and SU(5)", *Nucl. Phys. B* **193** (1981) 150, doi:10.1016/0550-3213(81)90522-8.

[20] R. K. Kaul and P. Majumdar, "Cancellation of quadratically divergent mass corrections in globally supersymmetric spontaneously broken gauge theories", *Nucl. Phys. B* **199** (1982) 36, doi:10.1016/0550-3213(82)90565-X.

[21] S. Dimopoulos and G. F. Giudice, "Naturalness constraints in supersymmetric theories with nonuniversal soft terms", *Phys. Lett. B* **357** (1995) 573, doi:10.1016/0370-2693(95)00961-J, arXiv:hep-ph/9507282.

[22] R. Barbieri and D. Pappadopulo, "S-particles at their naturalness limits", *JHEP* **10** (2009) 061, doi:10.1088/1126-6708/2009/10/061, arXiv:0906.4546.

[23] M. Papucci, J. T. Ruderman, and A. Weiler, "Natural SUSY endures", *JHEP* **09** (2012) 035, doi:10.1007/JHEP09(2012)035, arXiv:1110.6926.

[24] G. R. Farrar and P. Fayet, "Phenomenology of the production, decay, and detection of new hadronic states associated with supersymmetry", *Phys. Lett. B* **76** (1978) 575, doi:10.1016/0370-2693(78)90858-4.

[25] Particle Data Group, P. A. Zyla et al., "Review of particle physics", *Prog. Theor. Exp. Phys.* **2020** (2020) 083C01, doi:10.1093/ptep/ptaa104.

[26] S. Dimopoulos, M. Dine, S. Raby, and S. D. Thomas, "Experimental signatures of low-energy gauge mediated supersymmetry breaking", *Phys. Rev. Lett.* **76** (1996) 3494, doi:10.1103/PhysRevLett.76.3494, arXiv:hep-ph/9601367.

[27] K. T. Matchev and S. D. Thomas, "Higgs and Z boson signatures of supersymmetry", *Phys. Rev. D* **62** (2000) 077702, doi:10.1103/PhysRevD.62.077702, arXiv:hep-ph/9908482.

[28] N. Arkani-Hamed et al., "MARMOSET: The path from LHC data to the new standard model via on-shell effective theories", 2007. arXiv:hep-ph/0703088.

[29] J. Alwall, M.-P. Le, M. Lisanti, and J. G. Wacker, "Model-independent jets plus missing energy searches", *Phys. Rev. D* **79** (2009) 015005, doi:10.1103/PhysRevD.79.015005, arXiv:0809.3264.

[30] J. Alwall, P. Schuster, and N. Toro, "Simplified models for a first characterization of new physics at the LHC", *Phys. Rev. D* **79** (2009) 075020, doi:10.1103/PhysRevD.79.075020, arXiv:0810.3921.

[31] D. Alves et al., "Simplified models for LHC new physics searches", *J. Phys. G* **39** (2012) 105005, doi:10.1088/0954-3899/39/10/105005, arXiv:1105.2838.

[32] J. T. Ruderman and D. Shih, "General Neutralino NLSPs at the Early LHC", *JHEP* **08** (2012) 159, doi:10.1007/JHEP08(2012)159, arXiv:1103.6083.

[33] B. Fuks, M. Klasen, D. R. Lamprea, and M. Rothering, "Gaugino production in proton-proton collisions at a center-of-mass energy of 8 TeV", *JHEP* **10** (2012) 081, doi:10.1007/JHEP10(2012)081, arXiv:1207.2159.

[34] B. Fuks, M. Klasen, D. R. Lamprea, and M. Rothering, "Precision predictions for electroweak superpartner production at hadron colliders with RESUMMINO", *Eur. Phys. J. C* **73** (2013) 2480, doi:10.1140/epjc/s10052-013-2480-0, arXiv:1304.0790.

[35] H. Baer et al., "Natural SUSY with a bino- or wino-like LSP", *Phys. Rev. D* **91** (2015) 075005, doi:10.1103/PhysRevD.91.075005, arXiv:1501.06357.

[36] Z. Kang, P. Ko, and J. Li, "New Physics Opportunities in the Boosted Di-Higgs-Boson Plus Missing Transverse Energy Signature", *Phys. Rev. Lett.* **116** (2016) 131801, doi:10.1103/PhysRevLett.116.131801, arXiv:1504.04128.

[37] G. D. Kribs, A. Martin, T. S. Roy, and M. Spannowsky, "Discovering Higgs Bosons of the MSSM using Jet Substructure", *Phys. Rev. D* **82** (2010) 095012, doi:10.1103/PhysRevD.82.095012, arXiv:1006.1656.

[38] S. Gori, P. Schwaller, and C. E. M. Wagner, "Search for Higgs Bosons in SUSY Cascade Decays and Neutralino Dark Matter", *Phys. Rev. D* **83** (2011) 115022, doi:10.1103/PhysRevD.83.115022, arXiv:1103.4138.

[39] LHC Higgs Cross Section Working Group, "Handbook of LHC Higgs cross sections: 4. deciphering the nature of the Higgs sector", *CERN* (2016) doi:10.23731/CYRM-2017-002, arXiv:1610.07922.

[40] ATLAS Collaboration, "Search for supersymmetry in events with photons, bottom quarks, and missing transverse momentum in proton-proton collisions at a centre-of-mass energy of 7 TeV with the ATLAS detector", *Phys. Lett. B* **719** (2013) 261, doi:10.1016/j.physletb.2013.01.041, arXiv:1211.1167.

[41] ATLAS Collaboration, "Search for direct pair production of a chargino and a neutralino decaying to the 125 GeV Higgs boson in $\sqrt{s} = 8$ TeV pp collisions with the ATLAS detector", *Eur. Phys. J. C* **75** (2015) 208, doi:10.1140/epjc/s10052-015-3408-7, arXiv:1501.07110.

[42] ATLAS Collaboration, "Search for supersymmetry in final states with two same-sign or three leptons and jets using 36 fb^{-1} of $\sqrt{s} = 13$ TeV pp collision data with the ATLAS detector", *JHEP* **09** (2017) 084, doi:10.1007/JHEP09(2017)084, arXiv:1706.03731. [Erratum: JHEP 08, 121 (2019)].

[43] ATLAS Collaboration, "Search for new phenomena with large jet multiplicities and missing transverse momentum using large-radius jets and flavour-tagging at ATLAS in 13 TeV pp collisions", *JHEP* **12** (2017) 034, doi:10.1007/JHEP12(2017)034, arXiv:1708.02794.

[44] ATLAS Collaboration, "Search for squarks and gluinos in events with an isolated lepton, jets, and missing transverse momentum at $\sqrt{s} = 13$ TeV with the ATLAS detector", *Phys. Rev. D* **96** (2017) 112010, doi:10.1103/PhysRevD.96.112010, arXiv:1708.08232.

[45] ATLAS Collaboration, "Search for squarks and gluinos in final states with jets and missing transverse momentum using 36 fb^{-1} of $\sqrt{s} = 13$ TeV pp collision data with the ATLAS detector", *Phys. Rev. D* **97** (2018) 112001, doi:10.1103/PhysRevD.97.112001, arXiv:1712.02332.

[46] ATLAS Collaboration, "Search for electroweak production of supersymmetric states in scenarios with compressed mass spectra at $\sqrt{s} = 13$ TeV with the ATLAS detector", *Phys. Rev. D* **97** (2018) 052010, doi:10.1103/PhysRevD.97.052010, arXiv:1712.08119.

[47] ATLAS Collaboration, "Search for photonic signatures of gauge-mediated supersymmetry in 13 TeV pp collisions with the ATLAS detector", *Phys. Rev. D* **97** (2018) 092006, doi:10.1103/PhysRevD.97.092006, arXiv:1802.03158.

[48] ATLAS Collaboration, "Search for electroweak production of supersymmetric particles in final states with two or three leptons at $\sqrt{s} = 13$ TeV with the ATLAS detector", *Eur. Phys. J. C* **78** (2018) 995, doi:10.1140/epjc/s10052-018-6423-7, arXiv:1803.02762.

[49] ATLAS Collaboration, "Search for chargino-neutralino production using recursive jigsaw reconstruction in final states with two or three charged leptons in proton-proton collisions at $\sqrt{s} = 13$ TeV with the ATLAS detector", *Phys. Rev. D* **98** (2018) 092012, doi:10.1103/PhysRevD.98.092012, arXiv:1806.02293.

[50] ATLAS Collaboration, "Search for pair production of higgsinos in final states with at least three b-tagged jets in $\sqrt{s} = 13$ TeV pp collisions using the ATLAS detector", *Phys. Rev. D* **98** (2018) 092002, doi:10.1103/PhysRevD.98.092002, arXiv:1806.04030.

[51] ATLAS Collaboration, "Search for chargino and neutralino production in final states with a Higgs boson and missing transverse momentum at $\sqrt{s} = 13$ TeV with the ATLAS detector", *Phys. Rev. D* **100** (2019) 012006, doi:10.1103/PhysRevD.100.012006, arXiv:1812.09432.

[52] ATLAS Collaboration, "Search for electroweak production of charginos and sleptons decaying into final states with two leptons and missing transverse momentum in $\sqrt{s} = 13$ TeV pp collisions using the ATLAS detector", *Eur. Phys. J. C* **80** (2020) 123, doi:10.1140/epjc/s10052-019-7594-6, arXiv:1908.08215.

[53] ATLAS Collaboration, "Search for direct production of electroweakinos in final states with one lepton, missing transverse momentum and a Higgs boson decaying into two b-jets in pp collisions at $\sqrt{s} = 13$ TeV with the ATLAS detector", *Eur. Phys. J. C* **80** (2020) 691, doi:10.1140/epjc/s10052-020-8050-3, arXiv:1909.09226.

[54] ATLAS Collaboration, "Searches for electroweak production of supersymmetric particles with compressed mass spectra in $\sqrt{s} = 13$ TeV pp collisions with the ATLAS detector", *Phys. Rev. D* **101** (2020) 052005, doi:10.1103/PhysRevD.101.052005, arXiv:1911.12606.

[55] ATLAS Collaboration, "Search for chargino-neutralino production with mass splittings near the electroweak scale in three-lepton final states in $\sqrt{s}$=13 TeV pp collisions with the ATLAS detector", *Phys. Rev. D* **101** (2020) 072001, doi:10.1103/PhysRevD.101.072001, arXiv:1912.08479.

[56] ATLAS Collaboration, "Search for direct production of electroweakinos in final states with missing transverse momentum and a Higgs boson decaying into photons in pp collisions at $\sqrt{s}$ = 13 TeV with the ATLAS detector", *JHEP* **10** (2020) 005, doi:10.1007/JHEP10(2020)005, arXiv:2004.10894.

[57] ATLAS Collaboration, "Search for supersymmetry in events with four or more charged leptons in 139 fb^{-1} of $\sqrt{s} = 13$ TeV pp collisions with the ATLAS detector", arXiv:2103.11684.

[58] CMS Collaboration, "Searches for electroweak production of charginos, neutralinos, and sleptons decaying to leptons and W, Z, and Higgs bosons in pp collisions at 8 TeV", *Eur. Phys. J. C* **74** (2014) 3036, doi:10.1140/epjc/s10052-014-3036-7, arXiv:1405.7570.

[59] CMS Collaboration, "Search for top squark and higgsino production using diphoton Higgs boson decays", *Phys. Rev. Lett.* **112** (2014) 161802, doi:10.1103/PhysRevLett.112.161802, arXiv:1312.3310.

[60] CMS Collaboration, "Searches for electroweak neutralino and chargino production in channels with Higgs, Z, and W bosons in pp collisions at 8 TeV", *Phys. Rev. D* **90** (2014) 092007, doi:10.1103/PhysRevD.90.092007, arXiv:1409.3168.

[61] CMS Collaboration, "Search for physics beyond the standard model in events with two leptons of same sign, missing transverse momentum, and jets in proton–proton collisions at $\sqrt{s} = 13$ TeV", *Eur. Phys. J. C* **77** (2017) 578, doi:10.1140/epjc/s10052-017-5079-z, arXiv:1704.07323.

[62] CMS Collaboration, "Search for electroweak production of charginos and neutralinos in WH events in proton-proton collisions at $\sqrt{s} = 13$ TeV", *JHEP* **11** (2017) 029, doi:10.1007/JHEP11(2017)029, arXiv:1706.09933.

[63] CMS Collaboration, "Search for supersymmetry in events with at least one photon, missing transverse momentum, and large transverse event activity in proton-proton

collisions at $\sqrt{s} = 13$ TeV", *JHEP* **12** (2017) 142, doi:10.1007/JHEP12(2017)142, arXiv:1707.06193.

[64] CMS Collaboration, "Search for supersymmetry with Higgs boson to diphoton decays using the razor variables at $\sqrt{s} = 13$ TeV", *Phys. Lett. B* **779** (2018) 166, doi:10.1016/j.physletb.2017.12.069, arXiv:1709.00384.

[65] CMS Collaboration, "Search for Higgsino pair production in pp collisions at $\sqrt{s}$ = 13 TeV in final states with large missing transverse momentum and two Higgs bosons decaying via $H \to b\bar{b}$", *Phys. Rev. D* **97** (2018) 032007, doi:10.1103/PhysRevD.97.032007, arXiv:1709.04896.

[66] CMS Collaboration, "Combined search for electroweak production of charginos and neutralinos in proton-proton collisions at $\sqrt{s} = 13$ TeV", *JHEP* **03** (2018) 160, doi:10.1007/JHEP03(2018)160, arXiv:1801.03957.

[67] CMS Collaboration, "Search for new phenomena in final states with two opposite-charge, same-flavor leptons, jets, and missing transverse momentum in pp collisions at $\sqrt{s} = 13$ TeV", *JHEP* **03** (2018) 076, doi:10.1007/s13130-018-7845-2, arXiv:1709.08908.

[68] CMS Collaboration, "Search for supersymmetry in events with one lepton and multiple jets exploiting the angular correlation between the lepton and the missing transverse momentum in proton-proton collisions at $\sqrt{s} = 13$ TeV", *Phys. Lett. B* **780** (2018) 384, doi:10.1016/j.physletb.2018.03.028, arXiv:1709.09814.

[69] CMS Collaboration, "Search for supersymmetry in events with at least three electrons or muons, jets, and missing transverse momentum in proton-proton collisions at $\sqrt{s} = 13$ TeV", *JHEP* **02** (2018) 067, doi:10.1007/JHEP02(2018)067, arXiv:1710.09154.

[70] CMS Collaboration, "Search for gauge-mediated supersymmetry in events with at least one photon and missing transverse momentum in pp collisions at $\sqrt{s} = 13$ TeV", *Phys. Lett. B* **780** (2018) 118, doi:10.1016/j.physletb.2018.02.045, arXiv:1711.08008.

[71] CMS Collaboration, "Search for Physics Beyond the Standard Model in Events with High-Momentum Higgs Bosons and Missing Transverse Momentum in Proton-Proton Collisions at 13 TeV", *Phys. Rev. Lett.* **120** (2018) 241801, doi:10.1103/PhysRevLett.120.241801, arXiv:1712.08501.

[72] CMS Collaboration, "Search for new physics in events with two soft oppositely charged leptons and missing transverse momentum in proton-proton collisions at $\sqrt{s} = 13$ TeV", *Phys. Lett. B* **782** (2018) 440, doi:10.1016/j.physletb.2018.05.062, arXiv:1801.01846.

[73] CMS Collaboration, "Searches for pair production of charginos and top squarks in final states with two oppositely charged leptons in proton-proton collisions at $\sqrt{s} = 13$ TeV", *JHEP* **11** (2018) 079, doi:10.1007/JHEP11(2018)079, arXiv:1807.07799.

[74] CMS Collaboration, "Search for supersymmetry in events with a photon, a lepton, and missing transverse momentum in proton-proton collisions at $\sqrt{s} = 13$ TeV", *JHEP* **01** (2019) 154, doi:10.1007/JHEP01(2019)154, arXiv:1812.04066.

[75] CMS Collaboration, "Search for supersymmetry in events with a photon, jets, b -jets, and missing transverse momentum in proton–proton collisions at 13 TeV", *Eur. Phys. J. C* **79** (2019) 444, doi:10.1140/epjc/s10052-019-6926-x, arXiv:1901.06726.

[76] CMS Collaboration, "Search for supersymmetry in final states with photons and missing transverse momentum in proton-proton collisions at 13 TeV", *JHEP* **06** (2019) 143, doi:10.1007/JHEP06(2019)143, arXiv:1903.07070.

[77] CMS Collaboration, "Combined search for supersymmetry with photons in proton-proton collisions at $\sqrt{s} = 13$ TeV", *Phys. Lett. B* **801** (2020) 135183, doi:10.1016/j.physletb.2019.135183, arXiv:1907.00857.

[78] CMS Collaboration, "Search for supersymmetry using Higgs boson to diphoton decays at $\sqrt{s}$ = 13 TeV", *JHEP* **11** (2019) 109, doi:10.1007/JHEP11(2019)109, arXiv:1908.08500.

[79] CMS Collaboration, "Searches for physics beyond the standard model with the M_{T2} variable in hadronic final states with and without disappearing tracks in proton-proton collisions at $\sqrt{s} = 13$ TeV", *Eur. Phys. J. C* **80** (2020) 3, doi:10.1140/epjc/s10052-019-7493-x, arXiv:1909.03460.

[80] CMS Collaboration, "Search for physics beyond the standard model in events with jets and two same-sign or at least three charged leptons in proton-proton collisions at $\sqrt{s} =$ 13 TeV", *Eur. Phys. J. C* **80** (2020) 752, doi:10.1140/epjc/s10052-020-8168-3, arXiv:2001.10086.

[81] CMS Collaboration, "Search for supersymmetry in proton-proton collisions at $\sqrt{s} = 13$ TeV in events with high-momentum Z bosons and missing transverse momentum", *JHEP* **09** (2020) 149, doi:10.1007/JHEP09(2020)149, arXiv:2008.04422.

[82] CMS Collaboration, "Search for supersymmetry in final states with two oppositely charged same-flavor leptons and missing transverse momentum in proton-proton collisions at $\sqrt{s} = 13$ TeV", *JHEP* **04** (2021) 123, doi:10.1007/JHEP04(2021)123, arXiv:2012.08600.

[83] CMS Collaboration, "Search for electroweak production of charginos and neutralinos in proton-proton collisions at $\sqrt{s} = 13$ TeV", arXiv:2106.14246.

[84] CMS Collaboration, "The CMS experiment at the CERN LHC", *JINST* **3** (2008) S08004, doi:10.1088/1748-0221/3/08/S08004.

[85] CMS Collaboration, "Particle-flow reconstruction and global event description with the CMS detector", *JINST* **12** (2017) P10003, doi:10.1088/1748-0221/12/10/P10003, arXiv:1706.04965.

[86] M. Cacciari, G. P. Salam, and G. Soyez, "The anti-k_{t} jet clustering algorithm", *JHEP* **04** (2008) 063, doi:10.1088/1126-6708/2008/04/063, arXiv:0802.1189.

[87] M. Cacciari, G. P. Salam, and G. Soyez, "FastJet User Manual", *Eur. Phys. J. C* **72** (2012) 1896, doi:10.1140/epjc/s10052-012-1896-2, arXiv:1111.6097.

[88] CMS Collaboration, "Jet performance in pp collisions at $\sqrt{s} = 7$ TeV", CMS Physics Analysis Summary CMS-PAS-JME-10-003, 2010.

[89] CMS Collaboration, "Jet algorithms performance in 13 TeV data", CMS Physics Analysis Summary CMS-PAS-JME-16-003, 2017.

[90] CMS Collaboration, "Jet energy scale and resolution in the CMS experiment in pp collisions at 8 TeV", *JINST* **12** (2017) P02014, doi:10.1088/1748-0221/12/02/P02014, arXiv:1607.03663.

[91] M. Cacciari and G. P. Salam, "Pileup subtraction using jet areas", *Phys. Lett. B* **659** (2008) 119, doi:10.1016/j.physletb.2007.09.077, arXiv:0707.1378.

[92] D. Bertolini, P. Harris, M. Low, and N. Tran, "Pileup Per Particle Identification", *JHEP* **10** (2014) 059, doi:10.1007/JHEP10(2014)059, arXiv:1407.6013.

[93] CMS Collaboration, "Identification of heavy-flavour jets with the CMS detector in pp collisions at 13 TeV", *JINST* **13** (2018) P05011, doi:10.1088/1748-0221/13/05/P05011, arXiv:1712.07158.

[94] CMS Collaboration, "Performance of deep tagging algorithms for boosted double quark jet topology inproton-proton collisions at 13 tev with the phase-0 cms detector", CMS Detector Performance Note CMS-DP-2018-046, 2018.

[95] CMS Collaboration, "Performance of missing transverse momentum reconstruction in proton-proton collisions at $\sqrt{s} = 13$ TeV using the CMS detector", *JINST* **14** (2019) P07004, doi:10.1088/1748-0221/14/07/P07004, arXiv:1903.06078.

[96] CMS Collaboration, "Electron and photon reconstruction and identification with the CMS experiment at the CERN LHC", arXiv:2012.06888.

[97] CMS Collaboration, "Performance of the CMS muon detector and muon reconstruction with proton-proton collisions at $\sqrt{s} = 13$ TeV", *JINST* **13** (2018) P06015, doi:10.1088/1748-0221/13/06/P06015, arXiv:1804.04528.

[98] K. Rehermann and B. Tweedie, "Efficient Identification of Boosted Semileptonic Top Quarks at the LHC", *JHEP* **03** (2011) 059, doi:10.1007/JHEP03(2011)059, arXiv:1007.2221.

[99] J. Alwall et al., "The automated computation of tree-level and next-to-leading order differential cross sections, and their matching to parton shower simulations", *JHEP* **07** (2014) 079, doi:10.1007/JHEP07(2014)079, arXiv:1405.0301.

[100] J. Alwall et al., "Comparative study of various algorithms for the merging of parton showers and matrix elements in hadronic collisions", *Eur. Phys. J. C* **53** (2008) 473, doi:10.1140/epjc/s10052-007-0490-5, arXiv:0706.2569.

[101] R. Frederix and S. Frixione, "Merging meets matching in MC@NLO", *JHEP* **12** (2012) 061, doi:10.1007/JHEP12(2012)061, arXiv:1209.6215.

[102] P. Nason, "A new method for combining NLO QCD with shower Monte Carlo algorithms", *JHEP* **11** (2004) 040, doi:10.1088/1126-6708/2004/11/040, arXiv:hep-ph/0409146.

[103] S. Frixione, P. Nason, and C. Oleari, "Matching NLO QCD computations with parton shower simulations: the POWHEG method", *JHEP* **11** (2007) 070, doi:10.1088/1126-6708/2007/11/070, arXiv:0709.2092.

[104] S. Alioli, P. Nason, C. Oleari, and E. Re, "A general framework for implementing NLO calculations in shower Monte Carlo programs: the POWHEG BOX", *JHEP* **06** (2010) 043, doi:10.1007/JHEP06(2010)043, arXiv:1002.2581.

[105] S. Alioli, P. Nason, C. Oleari, and E. Re, "NLO single-top production matched with shower in POWHEG: s- and t-channel contributions", *JHEP* **09** (2009) 111, doi:10.1088/1126-6708/2009/09/111, arXiv:0907.4076. [Erratum: doi:10.1007/JHEP02(2010)011].

[106] E. Re, "Single-top Wt-channel production matched with parton showers using the POWHEG method", *Eur. Phys. J. C* **71** (2011) 1547, doi:10.1140/epjc/s10052-011-1547-z, arXiv:1009.2450.

[107] GEANT4 Collaboration, "GEANT4—a simulation toolkit", *Nucl. Instrum. Meth. A* **506** (2003) 250, doi:10.1016/S0168-9002(03)01368-8.

[108] T. Melia, P. Nason, R. Rontsch, and G. Zanderighi, "W^+W^-, WZ and ZZ production in the POWHEG BOX", *JHEP* **11** (2011) 078, doi:10.1007/JHEP11(2011)078, arXiv:1107.5051.

[109] M. Beneke, P. Falgari, S. Klein, and C. Schwinn, "Hadronic top-quark pair production with NNLL threshold resummation", *Nucl. Phys. B* **855** (2012) 695, doi:10.1016/j.nuclphysb.2011.10.021, arXiv:1109.1536.

[110] M. Cacciari et al., "Top-pair production at hadron colliders with next-to-next-to-leading logarithmic soft-gluon resummation", *Phys. Lett. B* **710** (2012) 612, doi:10.1016/j.physletb.2012.03.013, arXiv:1111.5869.

[111] P. Bärnreuther, M. Czakon, and A. Mitov, "Percent level precision physics at the Tevatron: First genuine NNLO QCD corrections to $q\bar{q} \to t\bar{t} + X$", *Phys. Rev. Lett.* **109** (2012) 132001, doi:10.1103/PhysRevLett.109.132001, arXiv:1204.5201.

[112] M. Czakon and A. Mitov, "NNLO corrections to top-pair production at hadron colliders: the all-fermionic scattering channels", *JHEP* **12** (2012) 054, doi:10.1007/JHEP12(2012)054, arXiv:1207.0236.

[113] M. Czakon and A. Mitov, "NNLO corrections to top pair production at hadron colliders: the quark-gluon reaction", *JHEP* **01** (2013) 080, doi:10.1007/JHEP01(2013)080, arXiv:1210.6832.

[114] M. Czakon, P. Fiedler, and A. Mitov, "Total top-quark pair-production cross section at hadron colliders through $O(\alpha_S^4)$", *Phys. Rev. Lett.* **110** (2013) 252004, doi:10.1103/PhysRevLett.110.252004, arXiv:1303.6254.

[115] R. Gavin, Y. Li, F. Petriello, and S. Quackenbush, "W physics at the LHC with FEWZ 2.1", *Comput. Phys. Commun.* **184** (2013) 208, doi:10.1016/j.cpc.2012.09.005, arXiv:1201.5896.

[116] R. Gavin, Y. Li, F. Petriello, and S. Quackenbush, "FEWZ 2.0: A code for hadronic Z production at next-to-next-to-leading order", *Comput. Phys. Commun.* **182** (2011) 2388, doi:10.1016/j.cpc.2011.06.008, arXiv:1011.3540.

[117] W. Beenakker, R. Höpker, M. Spira, and P. M. Zerwas, "Squark and gluino production at hadron colliders", *Nucl. Phys. B* **492** (1997) 51, doi:10.1016/S0550-3213(97)00084-9, arXiv:hep-ph/9610490.

[118] A. Kulesza and L. Motyka, "Threshold resummation for squark-antisquark and gluino-pair production at the LHC", *Phys. Rev. Lett.* **102** (2009) 111802, doi:10.1103/PhysRevLett.102.111802, arXiv:0807.2405.

[119] A. Kulesza and L. Motyka, "Soft gluon resummation for the production of gluino-gluino and squark-antisquark pairs at the LHC", *Phys. Rev. D* **80** (2009) 095004, doi:10.1103/PhysRevD.80.095004, arXiv:0905.4749.

[120] W. Beenakker et al., "Soft-gluon resummation for squark and gluino hadroproduction", *JHEP* **12** (2009) 041, doi:10.1088/1126-6708/2009/12/041, arXiv:0909.4418.

[121] W. Beenakker et al., "Squark and gluino hadroproduction", *Int. J. Mod. Phys. A* **26** (2011) 2637, doi:10.1142/S0217751X11053560, arXiv:1105.1110.

[122] W. Beenakker et al., "NNLL-fast: predictions for coloured supersymmetric particle production at the LHC with threshold and Coulomb resummation", *JHEP* **12** (2016) 133, doi:10.1007/JHEP12(2016)133, arXiv:1607.07741.

[123] W. Beenakker et al., "NNLL resummation for squark-antisquark pair production at the LHC", *JHEP* **01** (2012) 076, doi:10.1007/JHEP01(2012)076, arXiv:1110.2446.

[124] W. Beenakker et al., "Towards NNLL resummation: hard matching coefficients for squark and gluino hadroproduction", *JHEP* **10** (2013) 120, doi:10.1007/JHEP10(2013)120, arXiv:1304.6354.

[125] W. Beenakker et al., "NNLL resummation for squark and gluino production at the LHC", *JHEP* **12** (2014) 023, doi:10.1007/JHEP12(2014)023, arXiv:1404.3134.

[126] W. Beenakker et al., "Stop production at hadron colliders", *Nucl. Phys. B* **515** (1998) 3, doi:10.1016/S0550-3213(98)00014-5, arXiv:hep-ph/9710451.

[127] W. Beenakker et al., "Supersymmetric top and bottom squark production at hadron colliders", *JHEP* **08** (2010) 098, doi:10.1007/JHEP08(2010)098, arXiv:1006.4771.

[128] W. Beenakker et al., "NNLL resummation for stop pair-production at the LHC", *JHEP* **05** (2016) 153, doi:10.1007/JHEP05(2016)153, arXiv:1601.02954.

[129] S. Abdullin et al., "The fast simulation of the CMS detector at LHC", *J. Phys. Conf. Ser.* **331** (2011) 032049, doi:10.1088/1742-6596/331/3/032049.

[130] A. Giammanco, "The fast simulation of the CMS experiment", *J. Phys. Conf. Ser.* **513** (2014) 022012, doi:10.1088/1742-6596/513/2/022012.

[131] T. Sjöstrand et al., "An Introduction to PYTHIA 8.2", *Comput. Phys. Commun.* **191** (2015) 159, doi:10.1016/j.cpc.2015.01.024, arXiv:1410.3012.

[132] CMS Collaboration, "Event generator tunes obtained from underlying event and multiparton scattering measurements", *Eur. Phys. J. C* **76** (2016) 155, doi:10.1140/epjc/s10052-016-3988-x, arXiv:1512.00815.

[133] CMS Collaboration, "Extraction and validation of a new set of CMS PYTHIA8 tunes from underlying-event measurements", 2019. arXiv:1903.12179. Submitted to *Eur. Phys. J. C*.

[134] NNPDF Collaboration, "Parton distributions with QED corrections", *Nucl. Phys. B* **877** (2013) 290, doi:10.1016/j.nuclphysb.2013.10.010, arXiv:1308.0598.

[135] NNPDF Collaboration, "Parton distributions from high-precision collider data", *Eur. Phys. J. C* **77** (2017) 663, doi:10.1140/epjc/s10052-017-5199-5, arXiv:1706.00428.

[136] CMS Collaboration, "Search for Top-Squark Pair Production in the Single-Lepton Final State in pp Collisions at $\sqrt{s}$ = 8 TeV", *Eur. Phys. J. C* **73** (2013) 2677, doi:10.1140/epjc/s10052-013-2677-2, arXiv:1308.1586.

[137] CMS Collaboration, "The CMS trigger system", *JINST* **12** (2017) P01020, doi:10.1088/1748-0221/12/01/P01020, arXiv:1609.02366.

[138] CMS Collaboration, "Performance of the CMS Level-1 trigger in proton-proton collisions at $\sqrt{s} = 13$ TeV", *JINST* **15** (2020) P10017, doi:10.1088/1748-0221/15/10/P10017, arXiv:2006.10165.

[139] A. J. Larkoski, S. Marzani, G. Soyez, and J. Thaler, "Soft Drop", *JHEP* **05** (2014) 146, doi:10.1007/JHEP05(2014)146, arXiv:1402.2657.

[140] M. Dasgupta, A. Fregoso, S. Marzani, and G. P. Salam, "Towards an understanding of jet substructure", *JHEP* **09** (2013) 029, doi:10.1007/JHEP09(2013)029, arXiv:1307.0007.

[141] A. Kalogeropoulos and J. Alwall, "The SysCalc code: A tool to derive theoretical systematic uncertainties", 2018. arXiv:1801.08401.

[142] S. Catani, D. de Florian, M. Grazzini, and P. Nason, "Soft gluon resummation for Higgs boson production at hadron colliders", *JHEP* **07** (2003) 028, doi:10.1088/1126-6708/2003/07/028, arXiv:hep-ph/0306211.

[143] M. Cacciari et al., "The $\mathrm{t\bar{t}}$ cross-section at 1.8 TeV and 1.96 TeV: a study of the systematics due to parton densities and scale dependence", *JHEP* **04** (2004) 068, doi:10.1088/1126-6708/2004/04/068, arXiv:hep-ph/0303085.

[144] CMS Collaboration, "Measurement of the inelastic proton-proton cross section at $\sqrt{s} = 13$ TeV", *JHEP* **07** (2018) 161, doi:10.1007/JHEP07(2018)161, arXiv:1802.02613.

[145] CMS Collaboration, "Precision luminosity measurement in proton-proton collisions at $\sqrt{s} = 13$ TeV in 2015 and 2016 at CMS", 2021. arXiv:2104.01927. Submitted to *Eur. Phys. J. C*.

[146] CMS Collaboration, "CMS luminosity measurement for the 2017 data-taking period at $\sqrt{s} = 13$ TeV", CMS Physics Analysis Summary CMS-PAS-LUM-17-004, 2018.

[147] CMS Collaboration, "CMS luminosity measurement for the 2018 data-taking period at $\sqrt{s} = 13$ TeV", CMS Physics Analysis Summary CMS-PAS-LUM-18-002, 2019.

[148] G. Cowan, K. Cranmer, E. Gross, and O. Vitells, "Asymptotic formulae for likelihood-based tests of new physics", *Eur. Phys. J. C* **71** (2011) 1554, doi:10.1140/epjc/s10052-011-1554-0, arXiv:1007.1727. [Erratum: doi:10.1140/epjc/s10052-013-2501-z].

[149] T. Junk, "Confidence level computation for combining searches with small statistics", *Nucl. Instrum. Meth. A* **434** (1999) 435, doi:10.1016/S0168-9002(99)00498-2, arXiv:hep-ex/9902006.

[150] A. L. Read, "Presentation of search results: the CL_s technique", *J. Phys. G* **28** (2002) 2693, doi:10.1088/0954-3899/28/10/313.